Effect of Element Size on the Solution Accuracies of Finite-Element Heat Transfer and Thermal Stress Analyses of Space Shuttle Orbiter

William L. Ko and Timothy Olona

August 1987

NASA
National Aeronautics and
Space Administration

Effect of Element Size on the Solution Accuracies of Finite-Element Heat Transfer and Thermal Stress Analyses of Space Shuttle Orbiter

William L. Ko and Timothy Olona
Ames Research Center, Dryden Flight Research Facility, Edwards, California

1987

SUMMARY

The effect of element size on the solution accuracies of finite-element heat transfer and thermal stress analyses of space shuttle orbiter was investigated. Several structural performance and resizing (SPAR) thermal models and NASA structural analysis (NASTRAN) structural models were set up for the orbiter wing midspan bay 3. The thermal model was found to be the one that determines the limit of finite-element fineness because of the limitation of computational core space required for the radiation view factor calculations. The thermal stresses were found to be extremely sensitive to a slight variation of structural temperature distributions. The minimum degree of element fineness required for the thermal model to yield reasonably accurate solutions was established. The radiation view factor computation time was found to be insignificant compared with the total computer time required for the SPAR transient heat transfer analysis.

NOMENCLATURE

C	capacitance matrix
CQUAD2	quadrilateral membrane and bending element
CROD	two-node tension-compression-torsion element
C41	four-node forced convection element
E23	bar element for axial stiffness only
E25	zero length element used to elastically connect geometrically coincident joints
E31	triangular membrane element
E41	quadrilateral membrane element
E44	quadrilateral shear panel element
F_{ij}	view factor from element i to element j
FRSI	felt reusable surface insulation
H	convection load vector
HRSI	high-temperature reusable surface insulation
JLOC	joint location
K_h	convection matrix
K_k	conduction matrix
K_r	radiation matrix
K21	two-node line conduction element
K31	three-node area conduction element
K41	four-node area conduction element
K81	eight-node volume conduction element
NASTRAN	NASA structural analysis
Q	source load vector
R	radiation load vector
R31	three-node area radiation element
R41	four-node area radiation element
SIP	strain isolation pad
SPAR	structural performance and resizing
STS	space transportation system
T	absolute temperature, °R
TPS	thermal protection system
t	time, sec

1

x, y, z	rectangular Cartesian coordinates
X_0	station on x axis, in
Y_0	station on y axis, in
σ_x	normal stress in x direction (chordwise stress), ksi
σ_y	normal stress in y direction (spanwise stress), ksi
τ_{xy}, τ_{yz}	shear stresses, ksi

INTRODUCTION

In finite-element heat transfer analysis or finite-element stress analysis, it is well known that reduction of element sizes (or increase in element number) will improve the solution accuracy. For simple structures, the element sizes may be reduced sufficiently to obtain highly accurate solutions. However, for large complex structures, such as the space shuttle orbiter, the use of excessively fine elements in the finite-element models may result in unmanageable computations that exceed the memory capability of existing computers. This computational limitation is frequently encountered during radiation view factor computations in the three-dimensional finite-element heat transfer analysis of complex structures. Because of computational limitations in the past heat transfer analysis of the space shuttle orbiter, only small local regions of the orbiter structure were modeled. Several regions of the space shuttle were modeled by Ko, Quinn, and Gong. For the past several years, these finite-element models were used to calculate orbiter structural temperatures, which were correlated with the actual flight data during the initial orbit tests of the space shuttle Columbia (refs. 1 to 7). Recently, Gong, Ko, and Quinn (ref. 4) conducted a finite-element heat transfer analysis of the orbiter whole wing (fig. 1) using a thermal model with relatively coarse elements (fig. 2). A similar whole wing finite-element structural model was used by Ko and Fields (ref. 8) in the thermal stress analysis of the orbiter whole wing. Both the thermal model (fig. 2) and the corresponding structural model (fig. 3) set up for the orbiter whole wing were too coarse to give sufficiently accurate structural temperature and thermal stress distributions. Before modifying the existing wing models by increasing the number of joint locations to improve the solutions, it is necessary to determine the minimum number of joint locations required for the modified wing thermal model (the corresponding wing structural model requires far fewer joint locations) to give reasonably accurate structural temperature distributions without causing the radiation view factor computations to become unmanageable. This report describes (1) heat transfer and thermal stress analyses of a single bay at the orbiter wing midspan using several different thermal and structural models having different numbers of joint locations (or different element sizes), (2) the effect of element sizes on the accuracies of solutions, and (3) the minimum number of joint locations required for the single-bay model to give reasonably accurate solutions. The results of this report will form the basic criteria in remodeling the whole orbiter wing or modeling other types of hypersonic aircraft wings (hot structures).

WHOLE WING THERMAL AND STRUCTURAL MODELS

In finite-element thermal stress analysis of the space shuttle orbiter, the temperature input to the structural model for the calculation of thermal stresses is usually obtained from the results of finite-element (or finite-difference) heat transfer analysis using the corresponding thermal model. Since the thermal protection system (TPS) is not a major load-carrying structure, it is neglected in the structural model. Thus, the structural model has far fewer joint locations (JLOCs) than the corresponding thermal model. For the wing models, the thermal model contains 2289 JLOCs, while the structural model has only 232 JLOCs (see table 1). Even though the thermal model has only one degree of freedom (temperature), because of

2

the radiation view factor computations and the transient nature of heat transfer, the computer core space required by the thermal model is always many times more than that required for the structural model, which has six degrees of freedom. Thus, the thermal model is the one that limits how fine the element size can be reduced for improving the solutions.

ONE-CELL THERMAL MODELS

To study the improvement of structural temperature distributions by reducing the element sizes, and also to study the associated effort involved in the computations of radiation view factors, five structural performance and resizing (SPAR, ref. 9) finite-element thermal models (with different degrees of element fineness) were set up for the orbiter wing midspan bay 3 bounded by Y_0-226 and Y_0-254 (see fig. 1). The five SPAR thermal models A, B, C, D, and E are shown in figure 4. The thermal model A is set up to match the coarseness of the existing whole wing thermal model. The four-node area conduction (K41) elements were used to model the wing skins, spar webs, rib cap shear webs, room temperature vulcanized (RTV) rubber layers lying on both sides of the strain isolation pad (SIP), and TPS surface coatings. The aerodynamic surfaces for providing source heat generation were modeled with one layer of K41 elements of unit thickness. The spar caps, rib caps, and rib trusses were modeled with two-node line conduction (K21) elements. The TPS was modeled in 10 layers on the lower surface and 3 layers on the upper surface using eight-node volume conduction (K81) elements. The SIP layer was modeled with only one layer of K81 elements. The external and internal radiations were modeled by attaching a layer of four-node area radiation (R41) elements to the active radiation surfaces. The radiation into space was modeled with one R41 element of unit area. No radiation elements were attached to the surfaces of spar caps, rib caps, rib cap shear webs, and rib trusses because of small exposed areas. A layer of four-node forced convection (C41) elements were attached to the internal surfaces of the bay to model the internal convection of air resulting from the entrance of external cool air into the interior of the orbiter wing at 1400 sec after reentry (or at 100,000 ft altitude). The front and rear ends of the thermal models were insulated. Table 2 summarizes the sizes (joint location number, number of different types of elements) of the five SPAR thermal models A, B, C, D, and E.

Heat Input

The external heat inputs to the SPAR thermal models are shown in figure 5. These aerodynamic heating curves are associated with STS-5 flight trajectories and are taken from reference 4, which describes in detail the method of calculations of aerodynamic heating.

View Factors

The view factors used in the radiation to space were calculated by hand. However, for the internal radiation exchanges, the view factors were calculated by using a VIEW computer program, which is incorporated into the SPAR thermal analysis computer program (ref. 9).

For both the external and the internal thermal radiation exchanges, all the view factors were calculated from the equation (ref. 9)

$$A_i F_{ij} = A_j F_{ji} \tag{1}$$

where A_i is the surface area of radiation exchange element i and F_{ij} is the view factor, defined as the fraction of radiant heat leaving element i incident on element j. In the calculation of view factors for the external radiation exchanges (considering that element i represents the space element and element j any radiation exchange element on the wing surface), F_{ji} was taken to be unity; therefore, $F_{ij} = A_j/A_i$ according to equation (1).

Values of emissivity and reflectivity used to compute radiant heat fluxes are given in table 3. The initial temperature distribution used in the analysis was obtained from the actual flight data. In thermal modeling, the majority of the time was consumed in the computations of view factors.

Internal Forced Convection

After opening the landing gear door and the vents at the wing roots, external air enters the shuttle wing and induces convective heat transfer. The heat transfer coefficients used for C41 elements were calculated using the effective air flow velocities inside the wing, listed in table 4 (ref. 6).

Transient Thermal Solutions

The SPAR thermal analysis finite-element computer program was used in the calculation of temperature time histories at all joint locations of the thermal models. The SPAR program used the following approach to obtain transient thermal solutions.

The transient heat transfer matrix equation

$$(K_k + K_r + K_h)T + C\dot{T} = Q + R + H \tag{2}$$

where

K_k	is the conduction matrix,
K_r	the radiation matrix,
K_h	the convection matrix,
T	the absolute temperature,
C	the capacitance matrix,
Q	the source load vector,
R	the radiation load vector,
H	the convection load vector, and
$[\dot{\,}]$	denotes time derivative,

was integrated by assuming that the temperature vector T_{i+1} at time step t_{i+1} can be expressed as

$$T_{i+1} = T_i + \dot{T}_i \, \Delta t + \frac{1}{2!}\ddot{T}_i \, \Delta t^2 + \frac{1}{3!}\dddot{T}T_i \, \Delta t^3 + \cdots \tag{3}$$

where T_i is the temperature vector at time step t_i and Δt is the time increment. The vector $\dot{T}_i$ is determined directly from equation (2) as

$$\dot{T}_i = -C^{-1}(K_k + K_r + K_h)T_i + C^{-1}(Q + R + H) \tag{4}$$

Higher order derivatives are obtained by differentiating equation (2) according to the assumptions that (1) material properties are constant over Δt, (2) Q and H vary linearly with time, and (3) R is constant over Δt:

$$\ddot{T}_i = -C^{-1}(K_k + 4K_r + K_h)\dot{T}_i + C^{-1}(\dot{Q} + \dot{H}) \tag{5}$$

$$\dddot{T}T_i = -C^{-1}(K_k + 4K_r + K_h)\ddot{T}_i - 4C^{-1}\dot{K}_r\dot{T}_i \tag{6}$$

In the present computations, the Taylor series expansion (eq. (3)) was cut off after the third term. The pressure dependency of the TPS and SIP thermal properties was converted into time dependency based on the trajectory of the STS-5 flight.

Time-dependent properties were averaged over time intervals (RESET TIME), which were taken to be 25 sec. Temperature-dependent properties were evaluated at the temperatures computed at the beginning of each time interval. The values Q, $\dot{Q}$, and R were computed every 2 sec.

4

ONE-CELL STRUCTURAL MODELS

For the thermal stress analysis, the NASA structural analysis (NASTRAN, ref. 10) computer program was used because it can handle temperature-dependent material properties. The SPAR structural computer program lacks this capability. The five NASTRAN structural models (not shown) corresponding to the five SPAR thermal models A, B, C, D, and E (fig. 4) are essentially the same except that the TPS layers are removed in the NASTRAN structural models. Thus, each set of thermal and corresponding structural models have identical joint locations so that the temperature distribution obtained from the thermal model can be input directly to the corresponding structural model for the calculations of thermal stresses. The wing skins, spar webs, and rib cap shear webs were modeled with quadrilateral membrane and bending (CQUAD2) elements. The spar caps, rib caps, and rib trusses were represented with two-node tension-compression-torsion (CROD) elements. To approximate the deformation field of the midspan bay 3 when it is not detached from the whole wing, the following boundary conditions were imposed on the NASTRAN structural models.

1. Y_0-226 plane fixed—The grid points lying in the Y_0-226 plane have no displacements in the y direction but are free to move in the x and z directions. The rotations with respect to the x, y, and z axes are constrained.

2. Y_0-254 plane free—The grid points lying in the Y_0-254 plane are free to move in the x, y, and z directions. The rotations with respect to the x, y, and z axes are constrained.

The thermal loadings to the NASTRAN structural models were generated by using the structural temperature distributions calculated from the corresponding SPAR thermal models. Table 5 summarizes the sizes of the five NASTRAN structural models. Because the TPS is removed, the structural models have far fewer joint locations as compared with corresponding SPAR thermal models (see table 2).

RESULTS

Structural Temperatures

Figure 6 shows the time histories of the midbay TPS surface temperatures calculated by using different SPAR thermal models. The five temperature curves respectively associated with the thermal models A, B, C, D, and E are so close as to be pictorially undiscernable. This implies that the element sizes in the substructure have negligible effect on the TPS surface temperatures. The STS-5 flight data are also shown in figure 6 (solid circles) for comparison. Figure 7 shows the time histories of the structural temperatures in the midbay regions of the lower and upper wing skins calculated from different thermal models. The thermal models B, C, D, and E yielded almost identical skin temperatures in the midbay regions. However, the thermal model A gave slightly lower wing skin temperatures because of coarseness of the model. The STS-5 flight data are also shown in figure 7 (solid circles) for comparison. Figure 8 shows the three-dimensional distributions of the wing skin temperatures, at t = 1700 sec from reentry, over whole surfaces of the lower and upper wing skins, calculated from different thermal models. The roof-shaped wing skin temperature distributions given by thermal model A (fig. 8(a)) is inadequate to represent actual distributions of the wing skin temperatures. The dome-shaped wing skin temperature profiles calculated from the thermal models B, C, D, and E (fig. 8(b) to (e)) are caused by the existence of the spars and ribs, which function as heat sinks. The dome-shaped wing skin temperature profiles imply the degree of thermal stress buildup in the wing skins, as will be discussed in the following section.

Figure 9 shows the calculated structural temperature distributions in the plane Y_0-240 of bay 3 at $t = 1700$ sec from reentry. The thermal model A definitely yielded inaccurate solutions. The structural temperature distributions given by thermal models B, C, D, and E are quite close. Especially, the thermal

5

models D and E yielded very close structural temperature distributions. As shown in the following section, a slight difference in the structural temperature distributions obtained from different thermal models could cause a "marked" difference in the induced thermal stress distributions. The structural temperature gradients are steepest near the lower spar caps because the spar webs function as heat sinks. Figure 10 shows the spanwise distributions of the wing skin temperatures at cross section X_o1270 based on different thermal models. The thermal models B, C, and D yield almost identical structural temperature distributions because they have the same number of elements in the spanwise direction. The shapes of the skin temperature distributions given by model E approach circular arcs. The solutions given by the thermal model A are rather poor because of an insufficient number of elements. When the number of the finite elements is increased sufficiently, the ultimate structural temperature distributions in the midspan bay 3 look like the curves shown in figures 11 and 12. The curves in the figures were constructed by fitting the data points obtained from SPAR thermal model E with smooth continuous curves.

Thermal Stresses

Figures 13 to 15 respectively show the distributions of the chordwise stresses σ_x, spanwise stresses σ_y, and shear stresses τ_{xy} calculated using different NASTRAN structural models. Clearly the structural model A gave inaccurate stress predictions. For the wing lower skin, the models C and D give σ_y distribution with stress-release zone at the mid bay region (fig. 14(c) and (d)). The σ_y distribution given by model E (fig. 14(e)) exhibits two zones: (1) stress-release zone between $y = -240$ and $y = -254$ and (2) stress-increase zone between $y = -226$ and $y = -240$. Figure 16 shows distributions of the spanwise stress σ_y calculated by using different NASTRAN structural models. Notice that the thermal stresses are very sensitive to the finite-element sizes (or structural temperature distributions). The coarser models A and B yielded peak compression in the midbay regions of both lower and upper skins. However, as the number of elements increased (models C, D, and E), the shallow U-shaped distributions of σ_y in the lower skin shifted to shallow W-shaped distributions, and the peak compression regions moved near the spar webs. The slight stress release in the midbay region of the lower skin, based on the structural models C, D, and E, is due to the bulging of the wing skin (described later in this section). For the upper skin, the zone of slight stress release showed up only for the stress distributions calculated from models D and E. These stress releases in the midbay regions of the wing skins were never observed in the earlier thermal stress analysis, which ignored the three-dimensional deformations of the orbiter skins (that is, skin-bulging effect). Figure 17 shows the distributions of chordwise stresses σ_x calculated from the five structural models. Again, the solution given by the model A is quite poor. The distributions of σ_x given by the structural models B, C, and D (all of which have four elements in the spanwise direction) are quite close. The structural model E, which has eight elements in the spanwise direction, gave a magnitude of peak compressional stress about 1.2 ksi above those predicted from the structural models B, C, and D. The marked difference in the σ_x distribution given by model E and those given by models B, C, and D is due to the existence of a stress-increase zone, which appeared only in model E. Unlike the distribution of σ_y (fig. 16), the distributions of σ_x calculated from all structural models did not exhibit stress release effects in the midbay regions of the wing skins. The magnitude of thermal stress σ_x (either in tension or compression) is higher than that of thermal stress σ_y shown in figure 16. Thus, σ_x is more critical than σ_y because the buckling strength of the wing skin in the x direction (normal to the hat stringers) is lower than that in the y direction (parallel to the hat stringers). The orbiter wing skin buckling stresses are in the neighborhood of $\sigma_x = -12$ ksi (normal to hat stringers) and $\sigma_y = -25$ ksi (parallel to hat stringers).

Figure 18 shows the distributions of shear stresses τ_{xy} and τ_{yz} in the cross section Y_0-252 (plane of highest shear) predicted from different NASTRAN structural models. The high shear-stress regions are near the lower spar caps.

6

When the number of finite elements is increased sufficiently, the ultimate distributions of the thermal stresses in the midspan bay 3 will look like the curves shown in figures 19 to 21. Those curves in the figures were constructed by fitting the data points obtained from NASTRAN structural models E with smooth continuous curves. Figure 22 shows the deformed shape of the orbiter wing midspan bay 3 due to STS-5 thermal loading. The front half of the wing lower skin bulged inwardly, but the rear half bulged outwardly; almost the entire wing upper skin bulged outwardly with more severe deformations in the front half region.

Computation Time

Table 6 summarizes the number of internal radiation view factors F_{ij} needed for different SPAR thermal models, the total computation time used in the transient heat transfer analyses associated with each thermal model, and the radiation view factor computation time. The data shown in table 6 are plotted in figure 23. Both the SPAR computation time and the number of internal radiation view factors appear to increase almost exponentially with the increase in the number of JLOCs. However, the time required for the radiation view factor computations turned out to be insignificant compared with the total SPAR computation time. The curves in figure 23 show how fast the computational "barrier" will be reached by accelerating the increase in the number of JLOCs.

CONCLUSIONS

Finite-element heat transfer and thermal stress analyses were performed on the space shuttle wing midspan bay 3 using several finite-element models of different degrees of element fineness. The effect of element sizes on the solution accuracy was investigated in great detail. The results of the analyses are summarized as follows:

1. The finite-element model A (thermal or structural), which has the same coarseness as the earlier whole wing model, is too coarse to yield satisfactory solutions.

2. The structural temperature distribution over the wing skin (lower or upper) surface of one bay was "dome" shaped and induced more severe thermal stresses in the chordwise direction than in the spanwise direction. The induced thermal stresses were very sensitive to slight variation of structural temperature distributions.

3. The structural models with finer elements yielded spanwise stress distributions exhibiting a stress release zone (due to skin bulging) at the midbay region of the wing skin (lower or upper), and the peak wing skin compression occurred near the spar caps. However, the coarser models gave the peak skin compression in the midbay region.

4. The front half of the wing lower skin bulged inwardly, but the rear half bulged outwardly. Almost the entire wing upper skin bulged outwardly with more severe deformations in the front half region.

5. For obtaining satisfactory thermal stress distributions, each wing skin (lower or upper) of one bay must be modeled with at least 8 elements in the spanwise direction (model E) and 10 elements in the chordwise direction (model D); each spar web must be modeled with at least 5 elements in the vertical directions (model D).

6. Both the computation time required for the SPAR transient heat transfer analysis and the number of view factors needed for internal radiation computations appeared to increase almost exponentially with the increase of the number of joint locations.

7

7. Even with the huge number of radiation view factor computations, the radiation view factor computation time was found to be insignificant compared with the total computer time required for the SPAR transient heat transfer analysis.

REFERENCES

1. Ko, William L.; Quinn, Robert D.; Gong, Leslie; Schuster, Lawrence S.; and Gonzales, David: Preflight Reentry Heat Transfer Analysis of Space Shuttle. AIAA-81-2382, Nov. 1981.

2. Ko, William L.; Quinn, Robert D.; Gong, Leslie; Schuster, Lawrence S.; and Gonzales, David: Reentry Heat Transfer Analysis of the Space Shuttle Orbiter. NASA CP-2216, 1982, pp. 295–325.

3. Gong, Leslie; Quinn, Robert D.; and Ko, William L.: Reentry Heating Analysis of Space Shuttle With Comparison of Flight Data. NASA CP-2216, 1982, pp. 271-294.

4. Gong, Leslie; Ko, William L.; and Quinn, Robert D.: Thermal Response of Space Shuttle Wing During Reentry Heating. AIAA-84-1761, June 1984. (Also published as NASA TM-85907, 1984.)

5. Ko, William L.; Quinn, Robert D.; and Gong, Leslie: Finite-Element Reentry Heat Transfer Analysis of Space Shuttle Orbiter. NASA TP-2657, 1986.

6. Ko, William L.; Quinn, Robert D.; and Gong, Leslie: Effect of Forced and Free Convections on Structural Temperatures of Space Shuttle Orbiter During Reentry Flight. AIAA-87-1600, June 1987.

7. Gong, Leslie; Ko, William L.; and Quinn, Robert D.: Comparison of Flight-Measured and Calculated Temperatures on Space Shuttle Orbiter. NASA TM-88278, 1987.

8. Ko, William L.; and Fields, Robert A.: Thermal Stress Analysis of Space Shuttle Orbiter Subjected to Reentry Aerodynamic Heating.

9. Marlowe, M.B.; Moore, R.A.; and Whetstone, W.D.: SPAR Thermal Analysis Processors Reference Manual, System Level 16, Volume 1: Program Execution. NASA CR-159162, 1979.

10. The NASTRAN User's Manual, Level 17.5. NASA SP-222(05), 1978.

TABLE 1. COMPARISON OF FINITE-ELEMENT THERMAL AND STRUCTURAL MODELS FOR SPACE SHUTTLE ORBITER WING

Thermal model		Structural model	
Feature	Number	Feature	Number
JLOCs	2289	JLOCs	232
K21 elements	1696	E23 elements	498
K31 elements	84	E25 elements	10
K41 elements	485	E31 elements	19
R31 elements	84	E41 elements	181
R41 elements	568	E44 elements	67

TABLE 2. SIZES OF SPAR THERMAL MODELS

SPAR thermal model	JLOCs	Element				
		K21	K41	K81	R41	C41
A	112	34	28	28	15	10
B	436	54	168	224	89	56
C	636	82	232	336	137	88
D	972	98	360	560	201	120
E	2076	146	848	1344	513	320

TABLE 3. EMISSIVITY AND REFLECTIVITY VALUES USED TO COMPUTE RADIANT HEAT FLUXES

Surface	Emissivity	Reflectivity
Windward	0.85	0.15
Leeward	0.80	0.20
Internal structure	0.667	0.333
Space	1.0	0

TABLE 4. EFFECTIVE AIR FLOW
VELOCITIES AND ASSOCIATED
HEAT TRANSFER COEFFICIENTS
FOR INTERNAL FORCED CONVECTION

Time (sec)	Effective air flow velocity (ft/sec)	Heat transfer coefficient (Btu/sec-in^2-°F)
1750	25	3.30×10^{-6}
1850	25	4.00×10^{-6}
2000	15	2.73×10^{-6}
3000	0	0.35×10^{-6a}

^{a}Heat transfer coefficient for natural convection.

TABLE 5. SIZES OF NASTRAN
STRUCTURAL MODELS

NASTRAN structural model	Grid	CQUAD2	CROD
A	24	18	54
B	82	72	54
C	140	112	74
D	196	160	90
E	429	368	132

TABLE 6. NUMBERS OF JOINT LOCATIONS AND INTERNAL RADIATION
VIEW FACTORS AND THERMAL ANALYSIS COMPUTATION TIME
ASSOCIATED WITH DIFFERENT SPAR THERMAL MODELS

SPAR thermal model	JLOCs	Number of internal radiation F_{ij}	SPAR computation time (min (hr))	F_{ij} computation time (min (hr))	Percent F_{ij} computation time
A	112	78	15 (0.25)	1.83 (0.031)	12.20
B	436	2,816	75 (1.25)	2.60 (0.043)	3.47
C	636	6,894	210 (3.5)	3.60 (0.060)	1.71
D	972	13,500	540 (9.0)	5.15 (0.086)	0.95
E	2076	93,869	1890 (31.5)	23.02 (0.384)	1.22

10
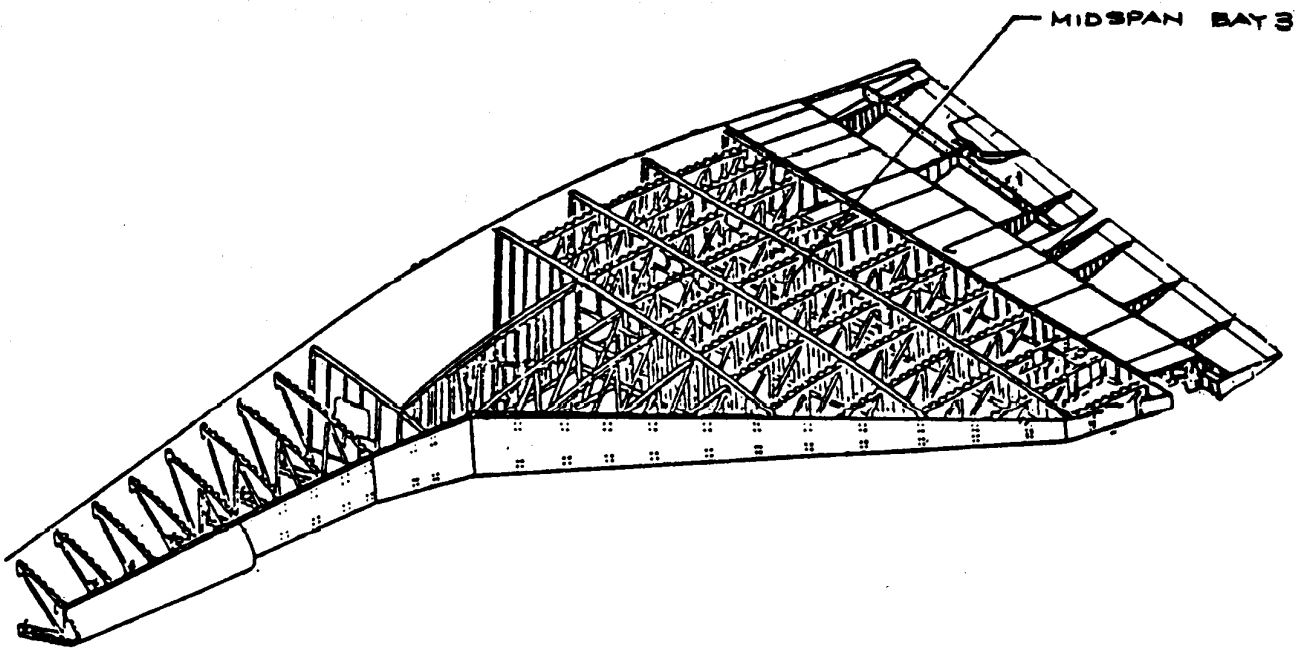
Figure 1. Space shuttle wing.
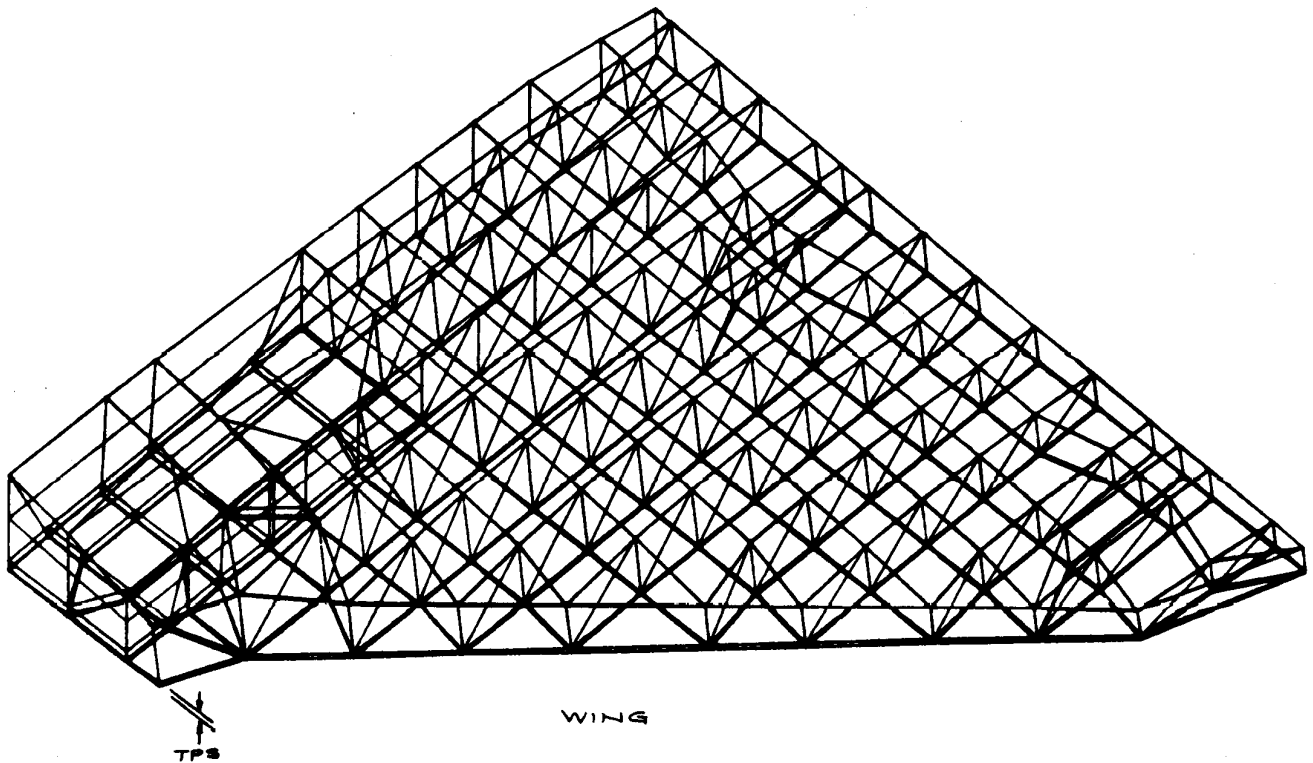
Figure 2. Space shuttle wing SPAR thermal model.
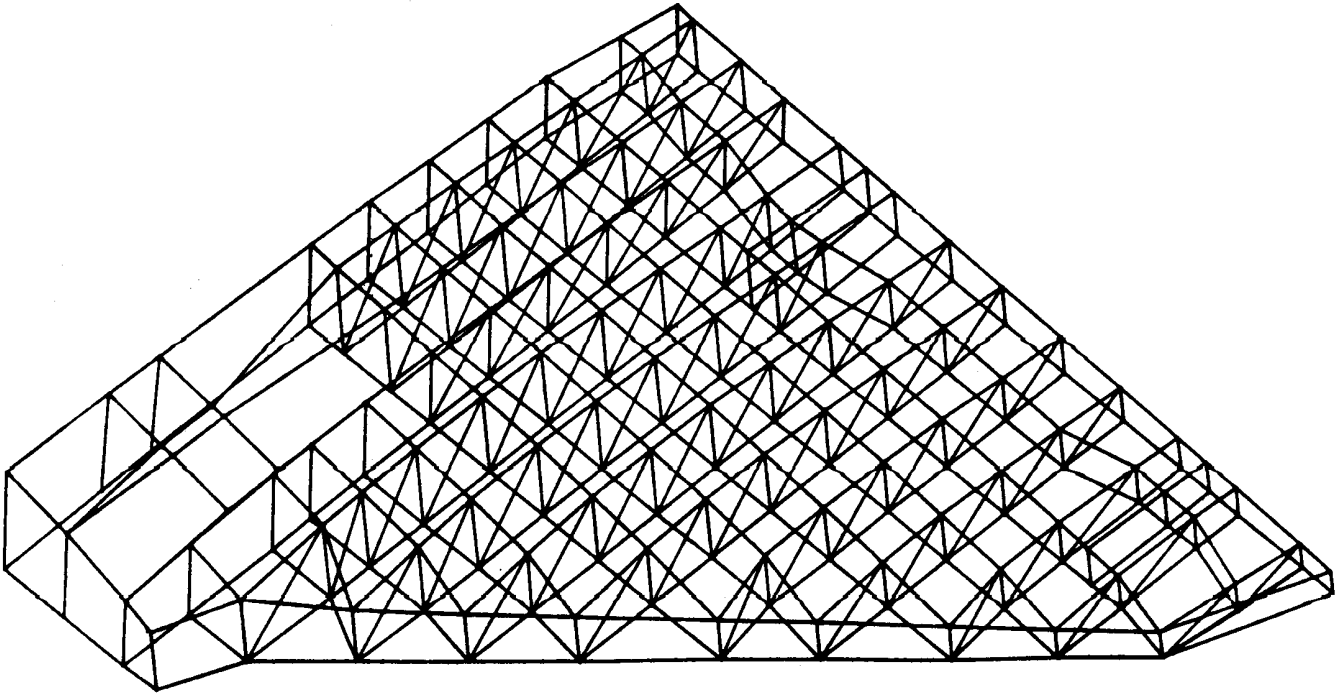
Figure 3. Space shuttle orbiter wing SPAR finite-element structural model. TPS, wheel well door, and landing gear excluded.
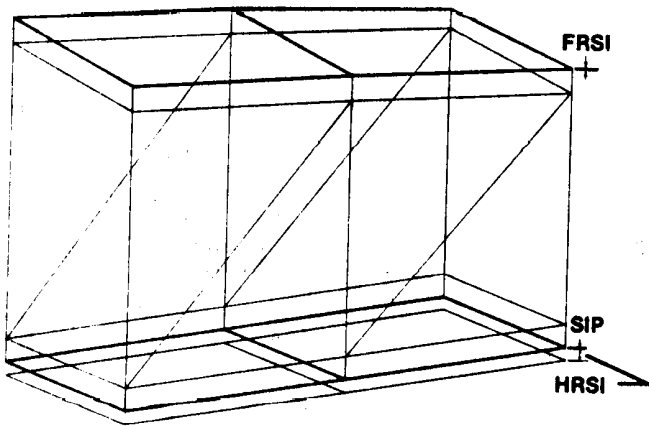
(a) Model A.
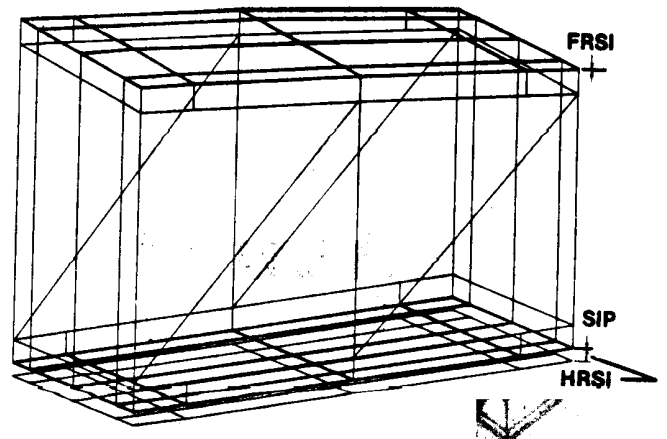
(b) Model B.

Figure 4. SPAR thermal models for bay 3 of orbiter wing bounded by Y_0-226 and Y_0-254. K81 elements for TPS and SIP not shown. TPS and SIP removed to convert to NASTRAN structural models.
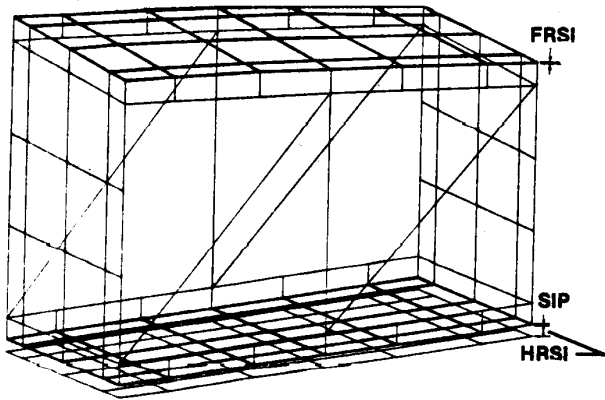
(c) Model C.
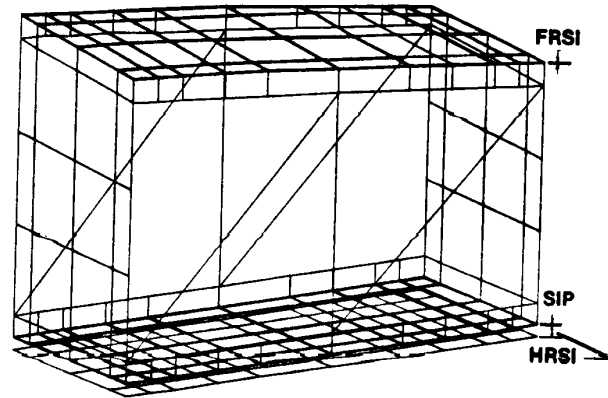
(d) Model D.
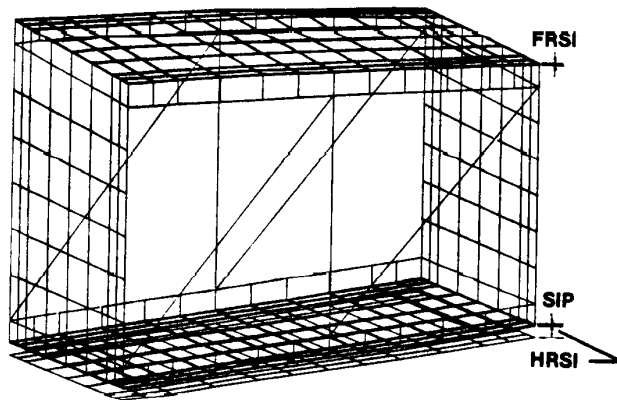
(e) Model E.

Figure 4. Concluded.

13
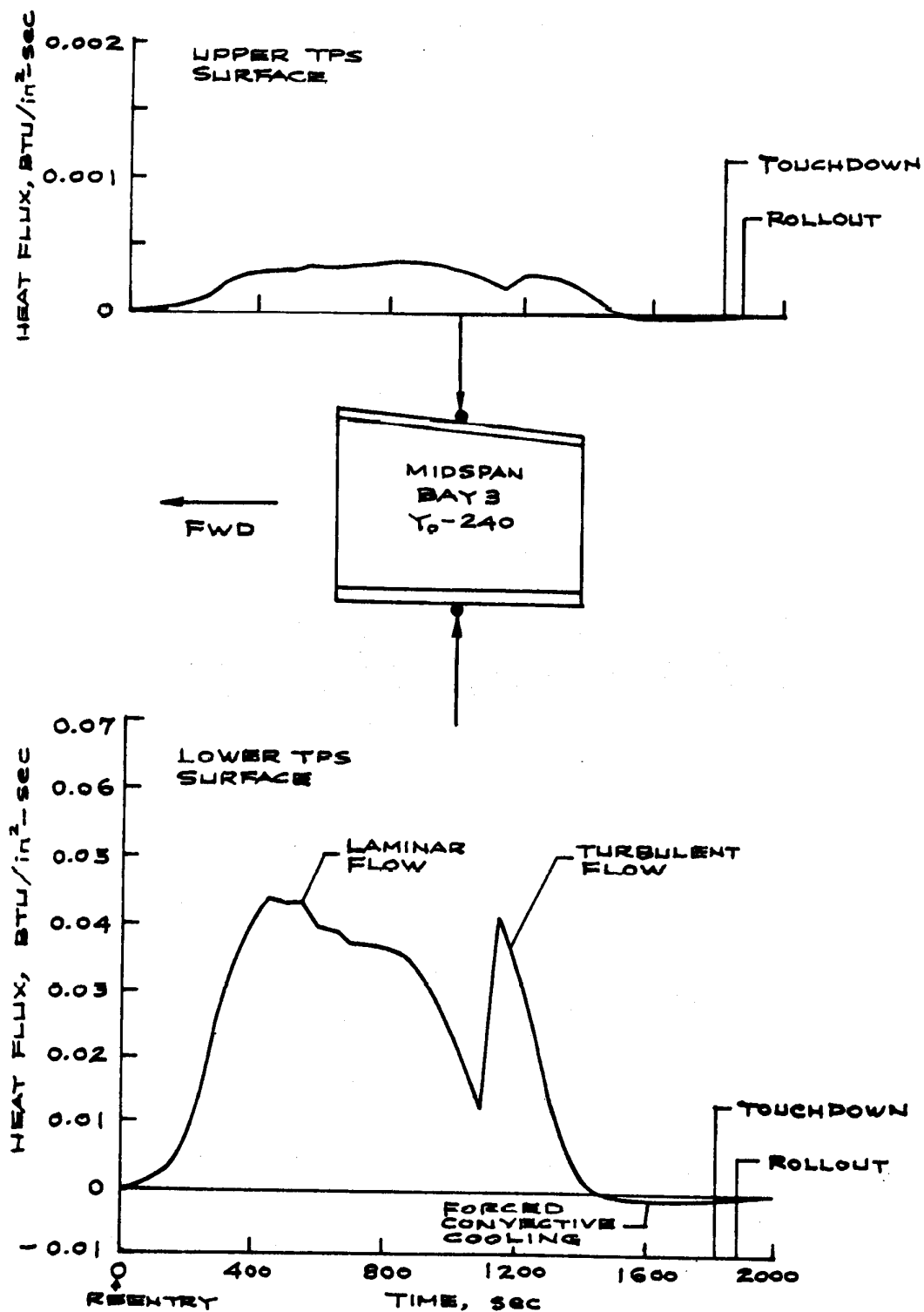
Figure 5. Surface heating rates at midspan bay 3 of orbiter wing; STS-5 flight.

14
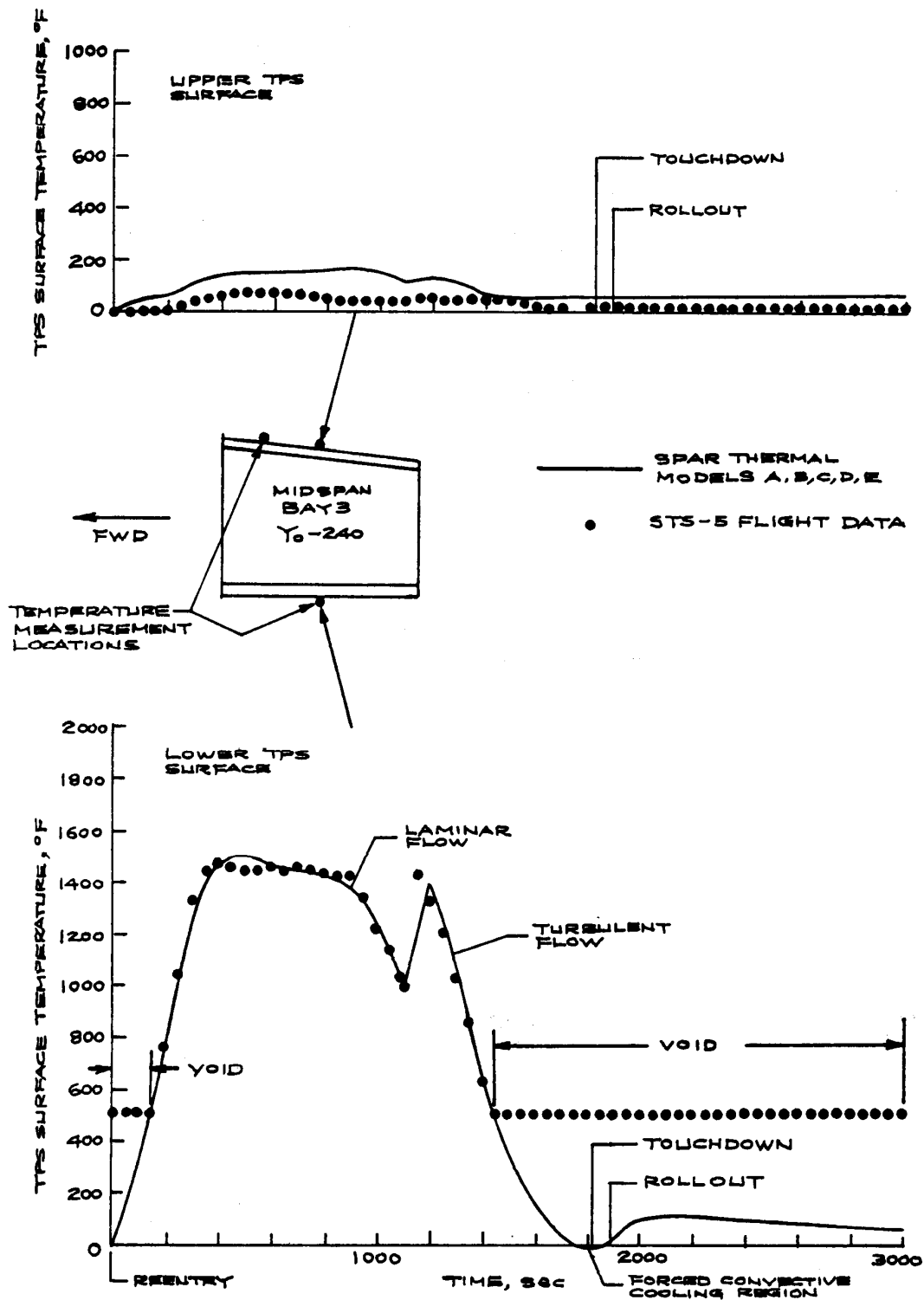
Figure 6. Time histories of TPS surface temperatures calculated using different SPAR thermal models; STS-5 flight.

15
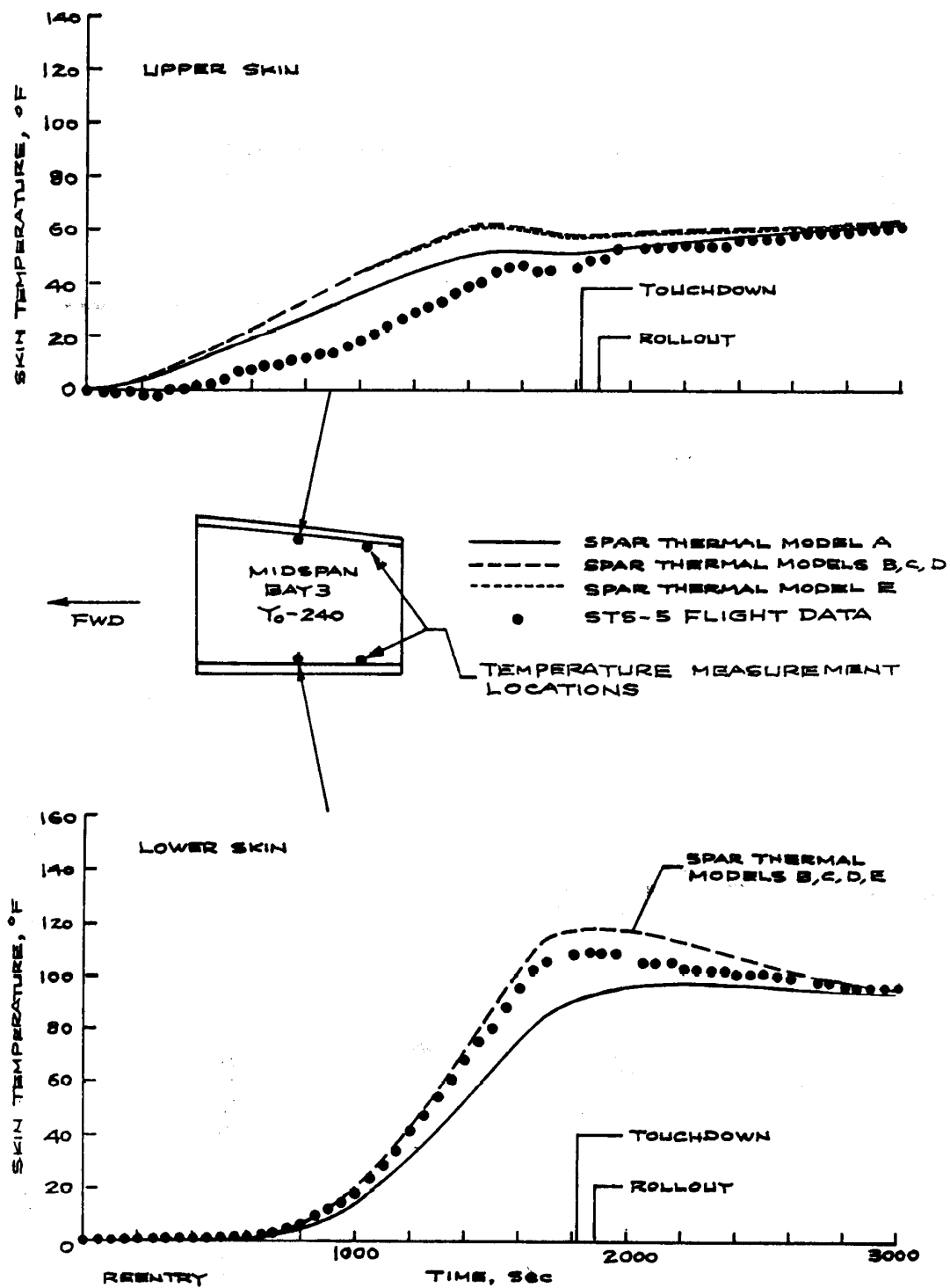
Figure 7. Time histories of orbiter wing skin temperatures calculated using different SPAR thermal models; STS-5 flight.
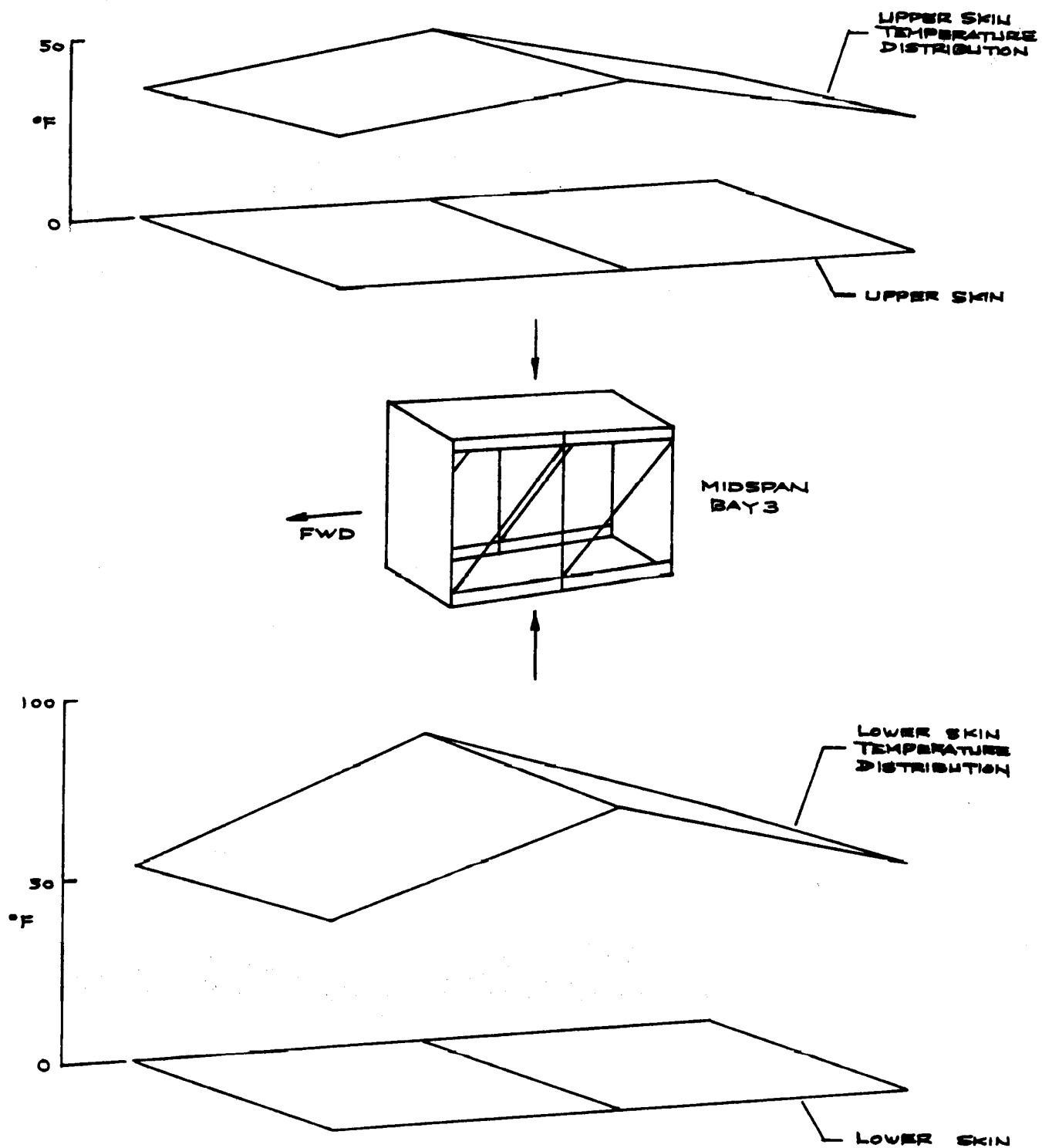
(a) SPAR thermal model A.

Figure 8. Distributions of orbiter wing skin temperatures at midspan bay 3; time = 1700 sec, STS-5 flight.

UPPER SKIN
TEMPERATURE
DISTRIBUTION

UPPER SKIN

MIDSPAN
BAY 3

FWD

LOWER SKIN
TEMPERATURE
DISTRIBUTION

LOWER SKIN
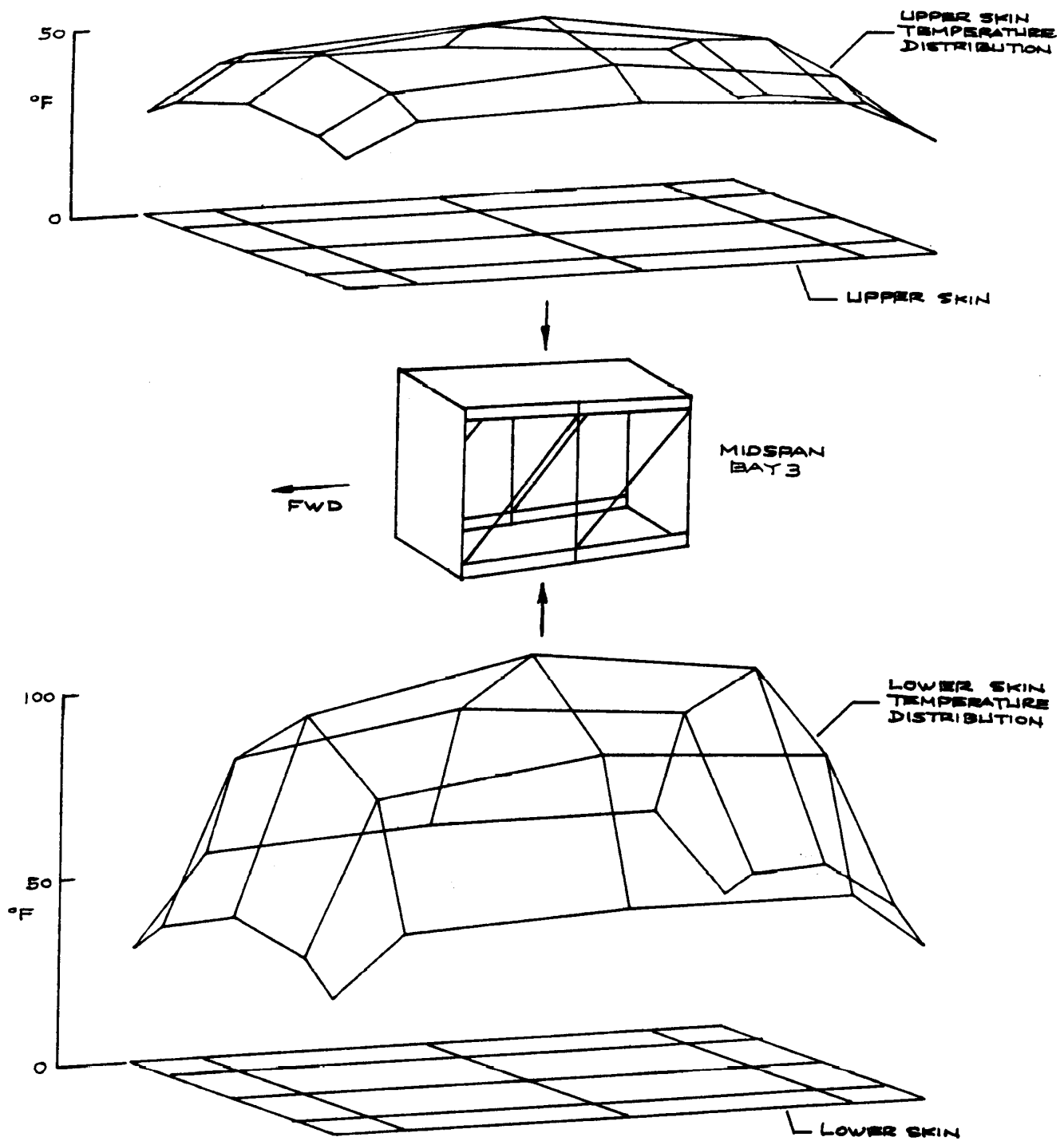
(b) SPAR thermal model B.

Figure 8. Continued.

18

UPPER SKIN
TEMPERATURE
DISTRIBUTION

UPPER SKIN

MIDSPAN
BAY 3

FWD

LOWER SKIN
TEMPERATURE
DISTRIBUTION

LOWER SKIN
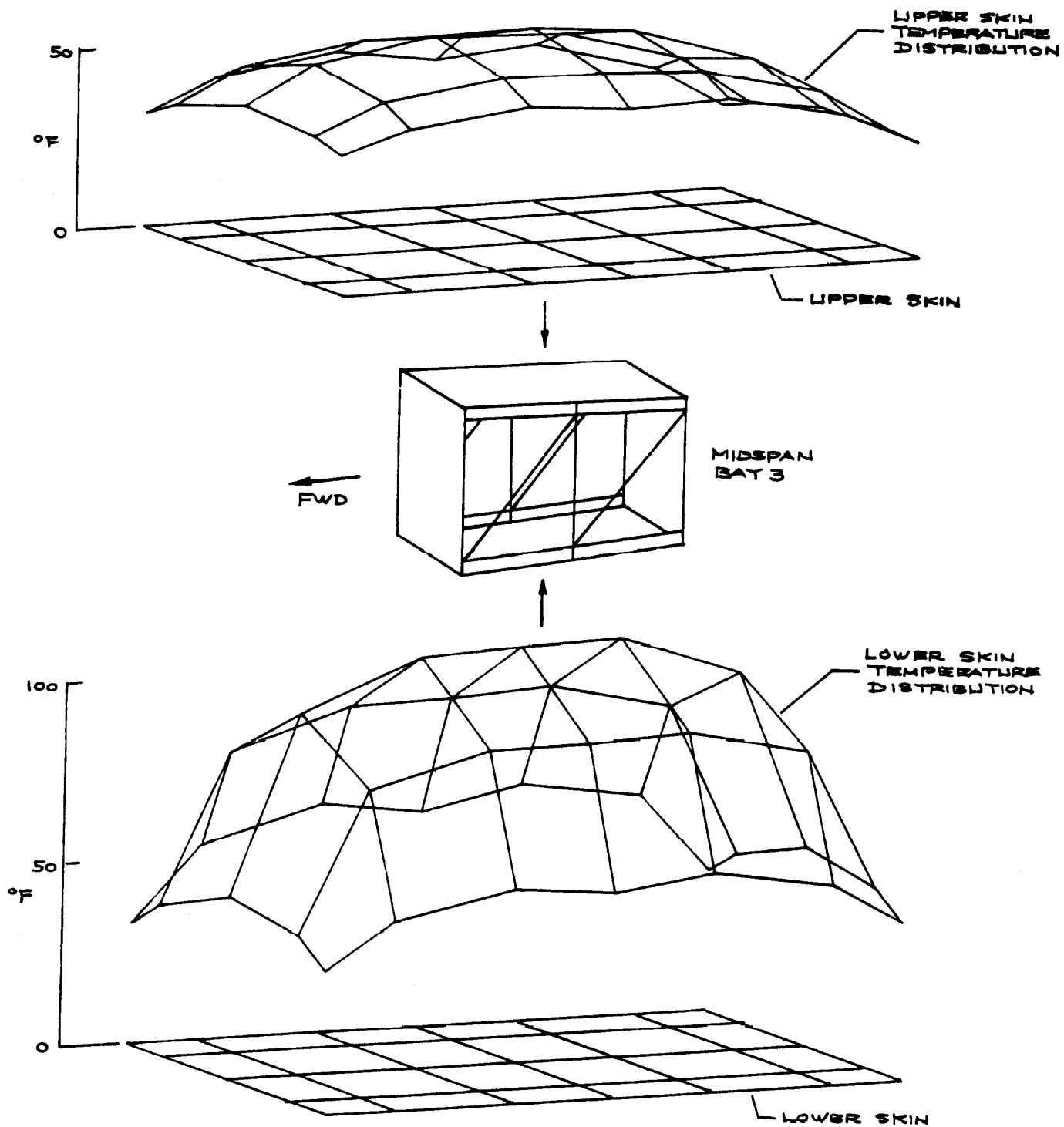
(c) SPAR thermal model C.

Figure 8. Continued.

19

UPPER SKIN TEMPERATURE DISTRIBUTION

UPPER SKIN

MIDSPAN BAY 3

FWD

LOWER SKIN TEMPERATURE DISTRIBUTION

LOWER SKIN
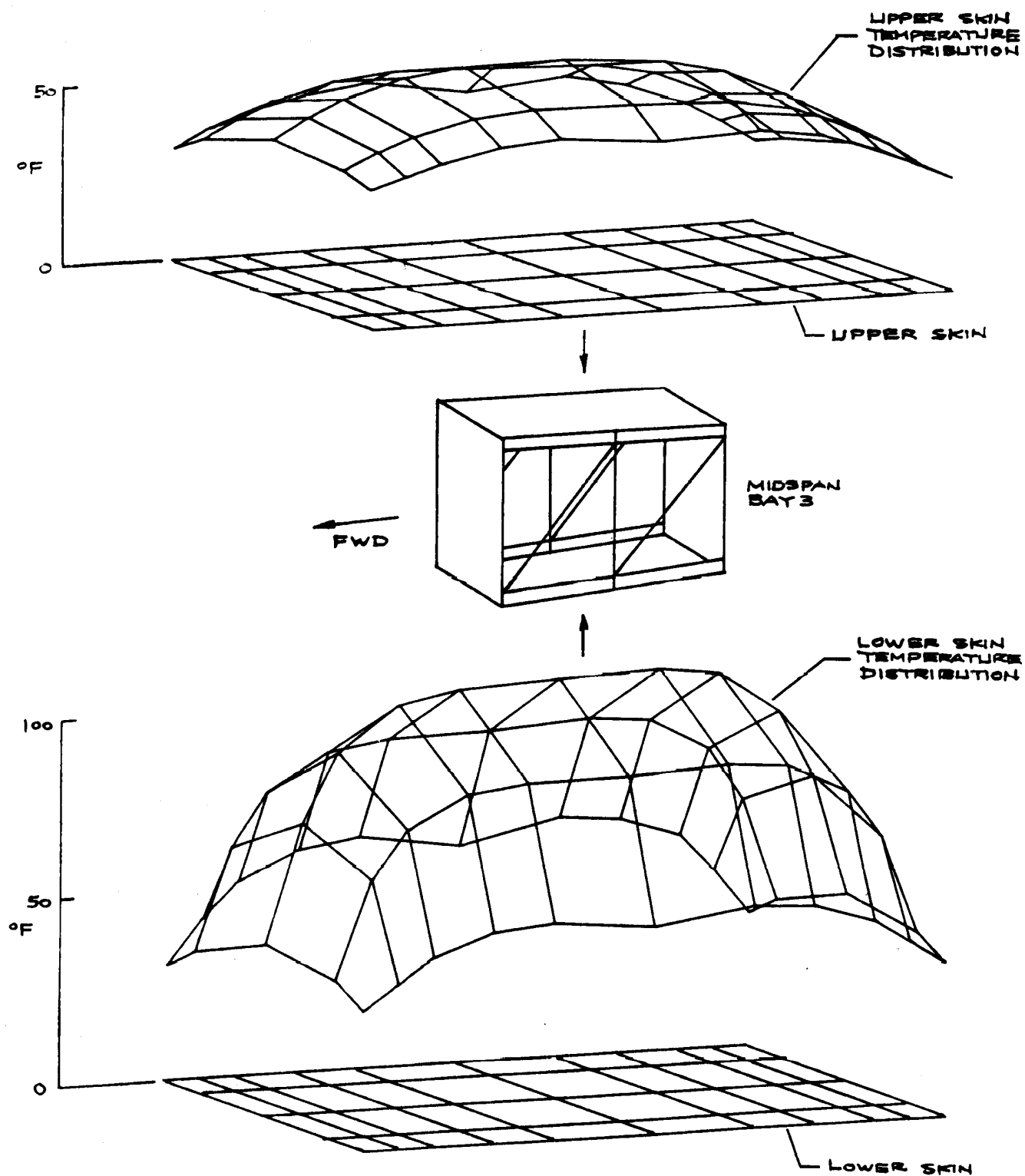
(d) SPAR thermal model D.

Figure 8. Continued.

20
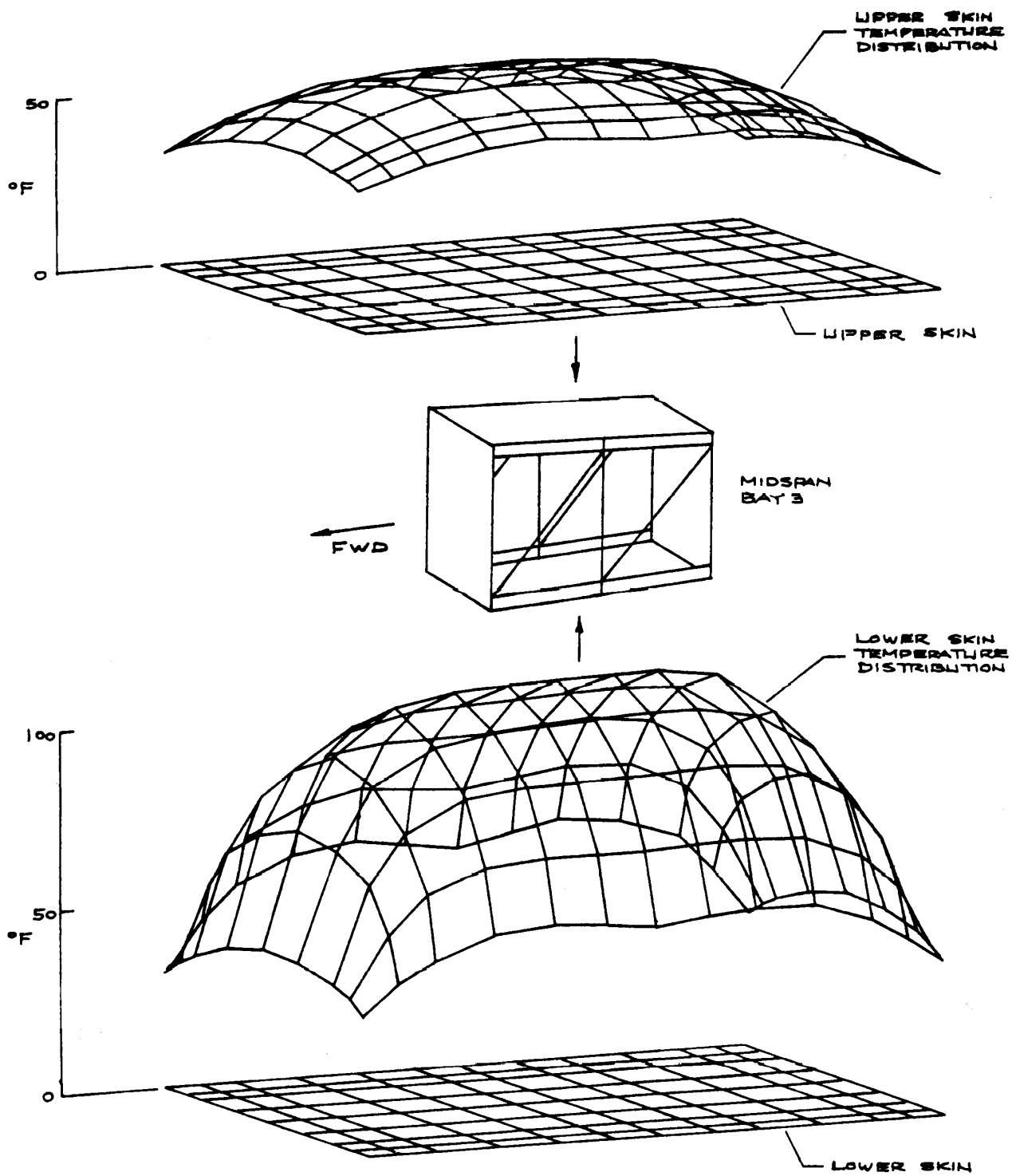
(e) SPAR thermal model E.

Figure 8. Concluded.
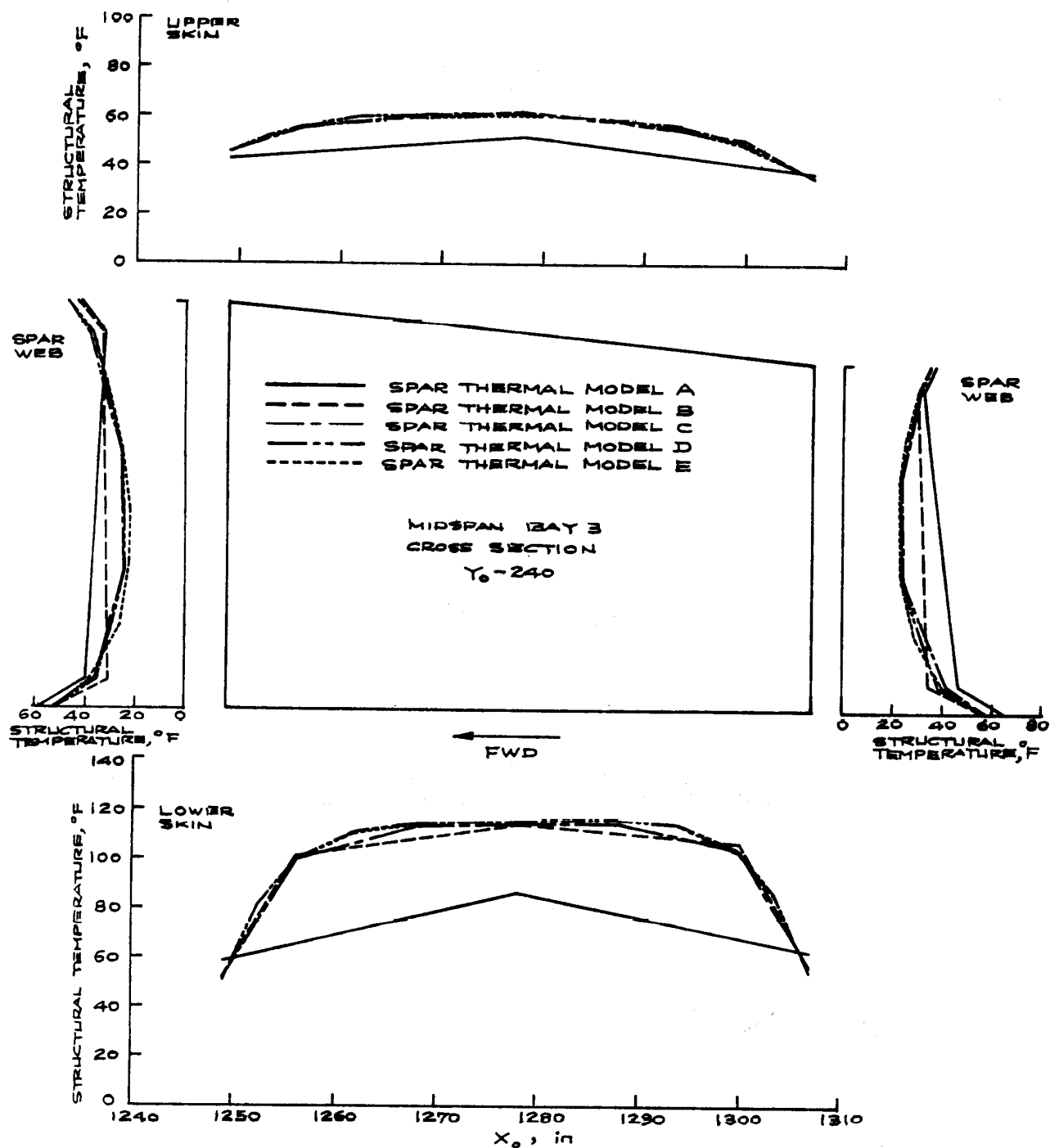
Figure 9. Structural temperature distributions in the Y_0-240 plane of orbiter wing midspan bay 3 calculated using different SPAR thermal models; time = 1700 sec, STS-5 flight.

UPPER
SKIN

STRUCTURAL TEMPERATURE, °F

100
80
60
40
20
0

SPAR THERMAL MODEL A
SPAR THERMAL MODELS B, C, D
SPAR THERMAL MODEL E

MIDSPAN BAY 3
CROSS SECTION
X_0 1278

INBOARD ←   → OUTBOARD

RIB AT
$Y_0 - 226$

RIB AT
$Y_0 - 254$

LOWER
SKIN

STRUCTURAL TEMPERATURE, °F

140
120
100
80
60
40
20
0

-225 -230 -235 -240 -245 -250 -255 -260

Y_0, in
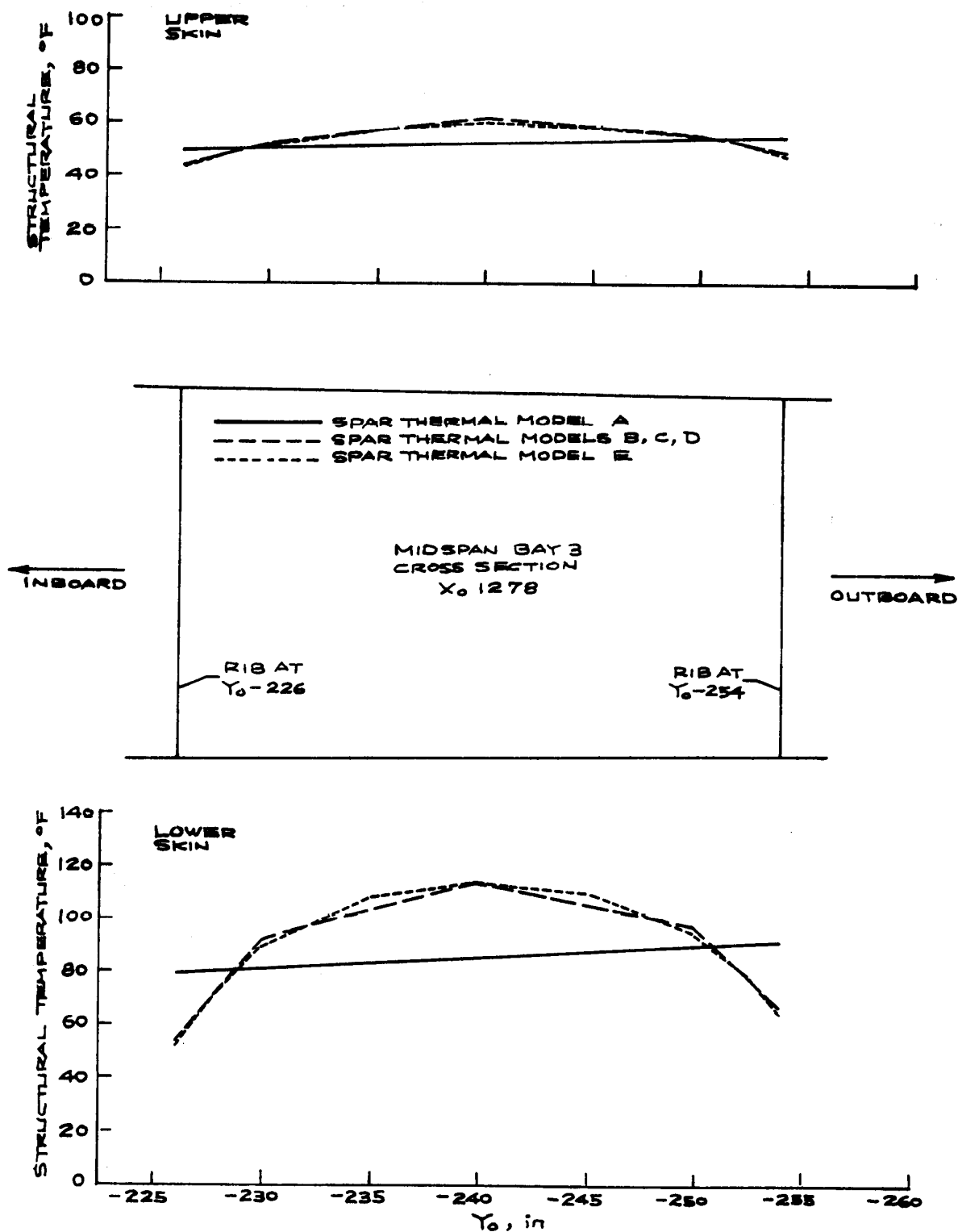
Figure 10. Spanwise distributions in the $X_0 1278$ plane of structural temperatures in orbiter wing midspan bay 3 calculated using different SPAR thermal models; time = 1700 sec, STS-5 flight.

23

UPPER SKIN

STRUCTURAL TEMPERATURE, °F

100
80
60
40
20
0

SPAR WEB

STRUCTURAL TEMPERATURE, °F
60 40 20 0

MIDSPAN BAY3
CROSS SECTION
Y₀-240

SPAR WEB

STRUCTURAL TEMPERATURE, °F
0 20 40 60 80

FWD

LOWER SKIN

STRUCTURAL TEMPERATURE, °F

120
100
80
60
40
20
0

1200 1250 1260 1270 1280 1290 1300 1310

X₀, in
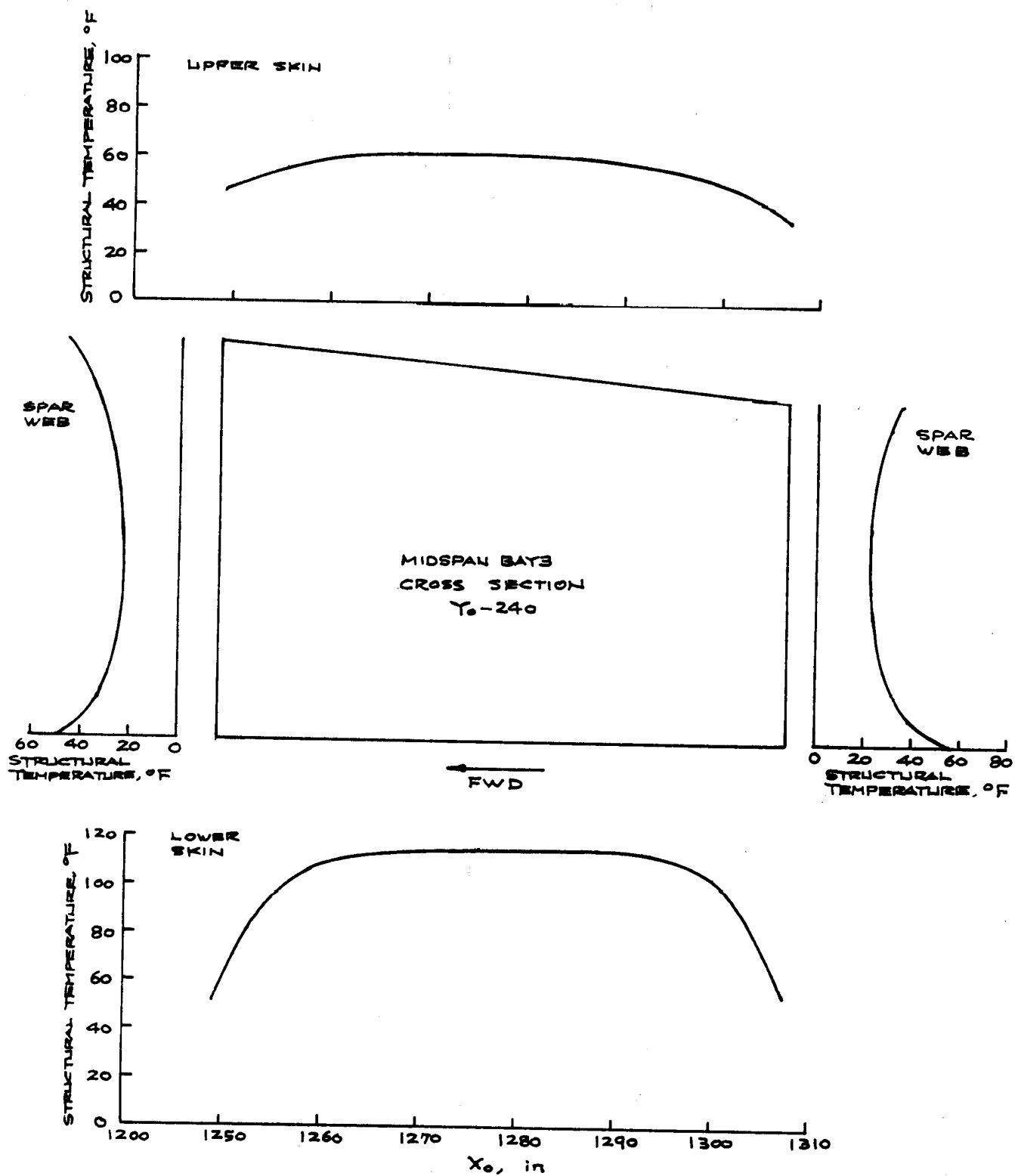
Figure 11. Continuous distributions in the Y_0-240 plane of structural temperatures based on SPAR thermal model E; time = 1700 sec, STS-5 flight.

24
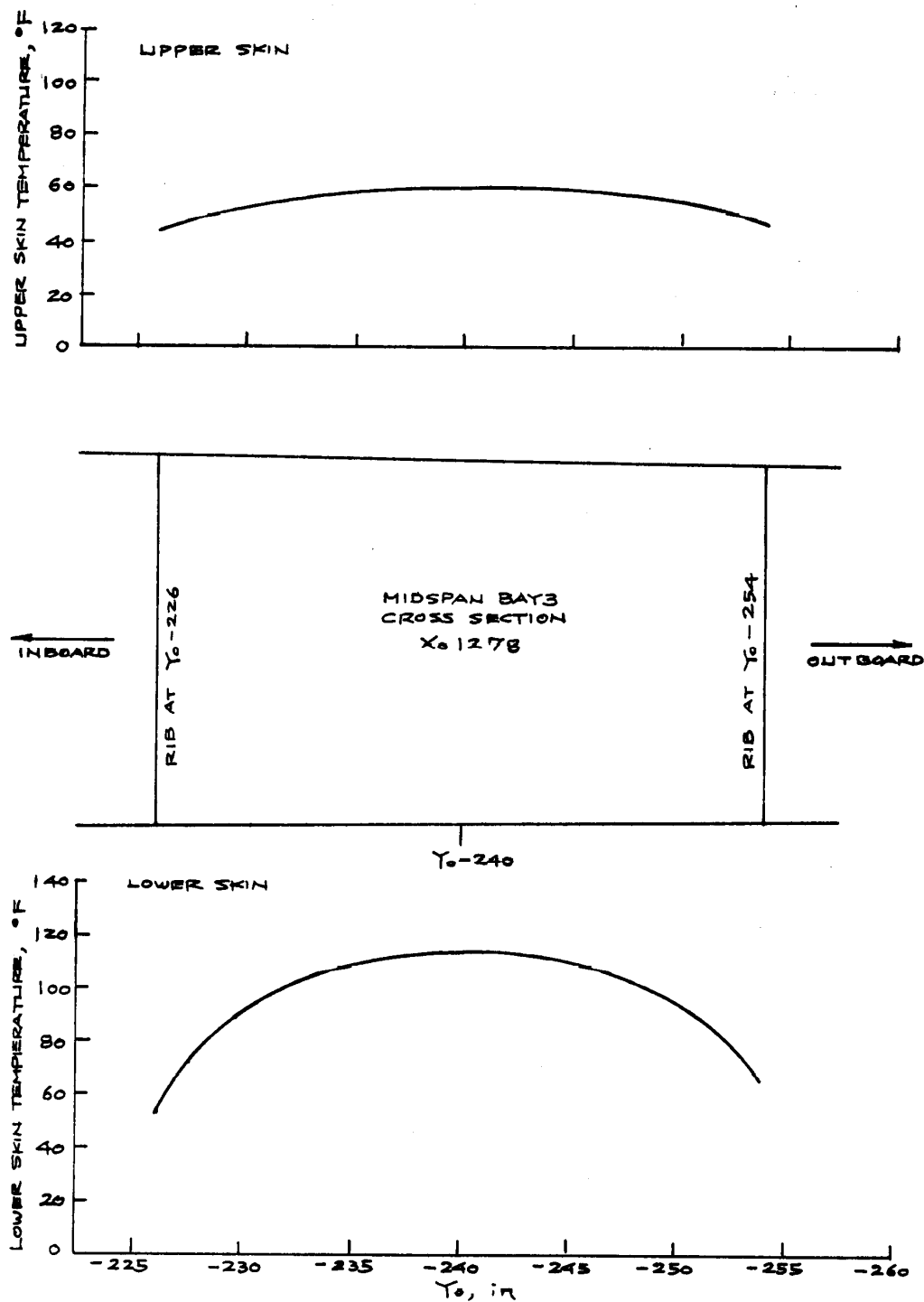
Figure 12. Continuous distributions of wing skin temperatures in the $X_0 1278$ plane based on thermal model E; time = 1700 sec, STS-5 flight.

25
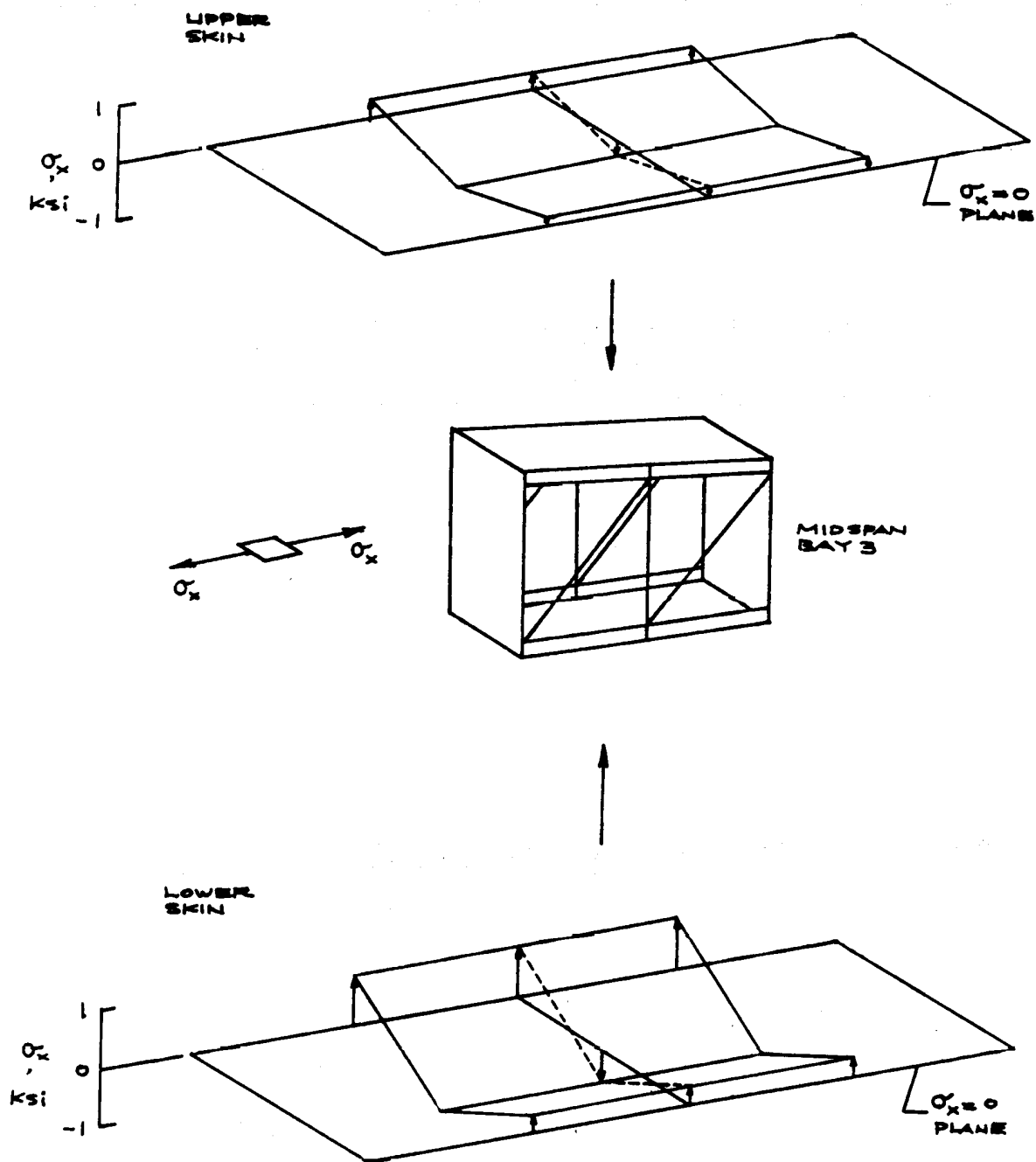
(a) NASTRAN structural model A.

Figure 13. Distributions of chordwise stress σ_x in orbiter wing skins at midspan bay 3; time = 1700 sec, STS-5 flight.
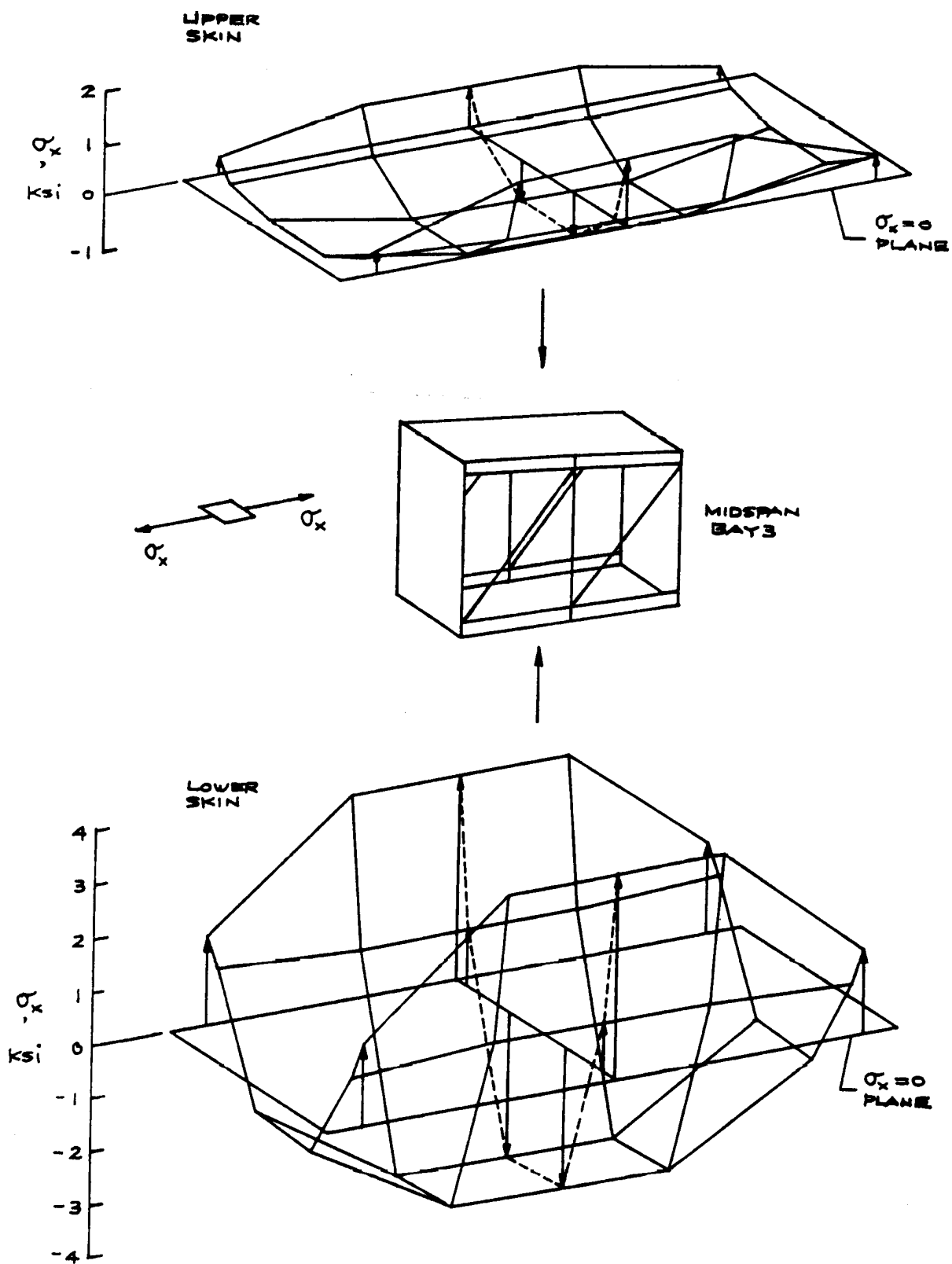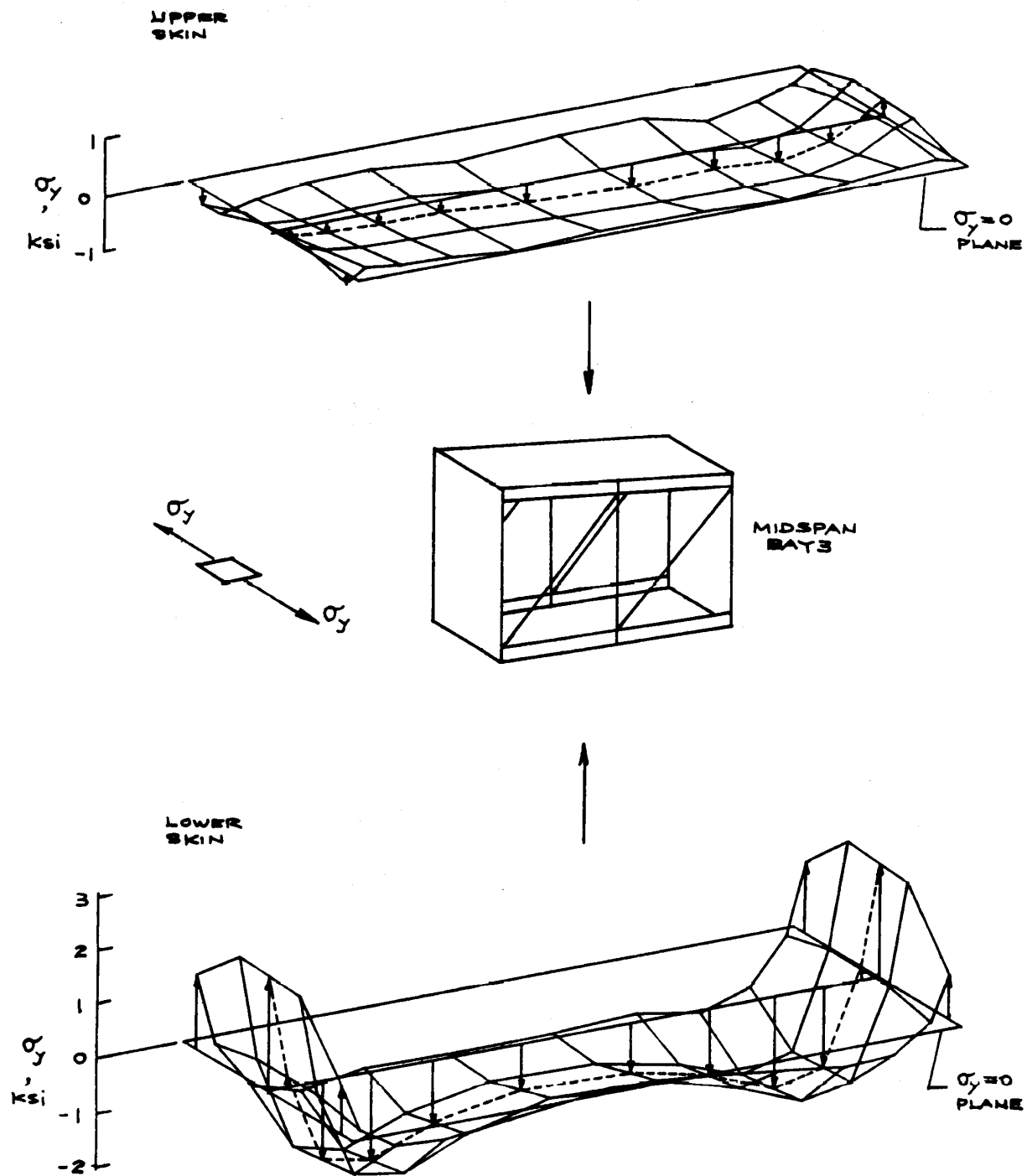
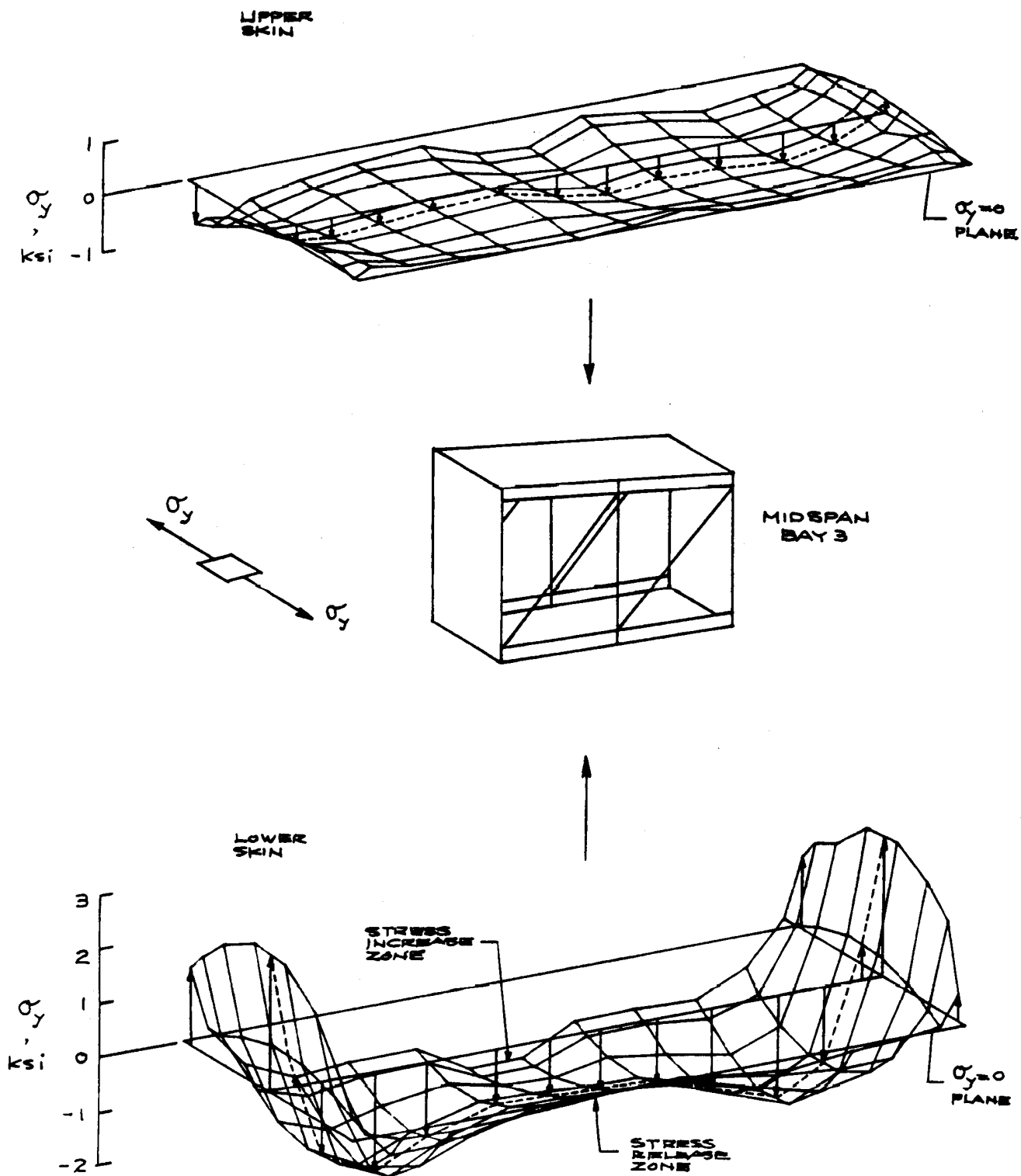*(b) NASTRAN structural model B.*

Figure 13. Continued.
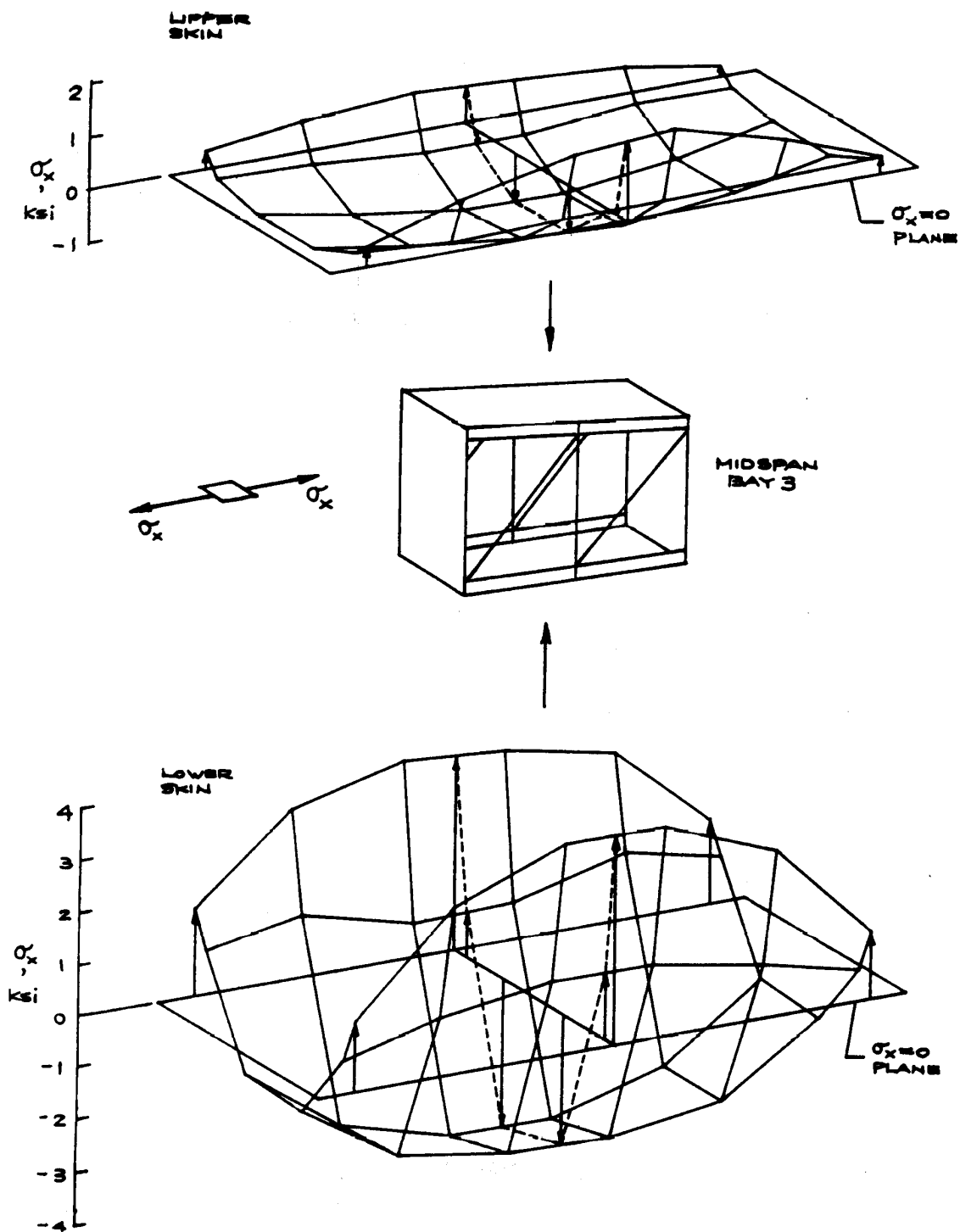
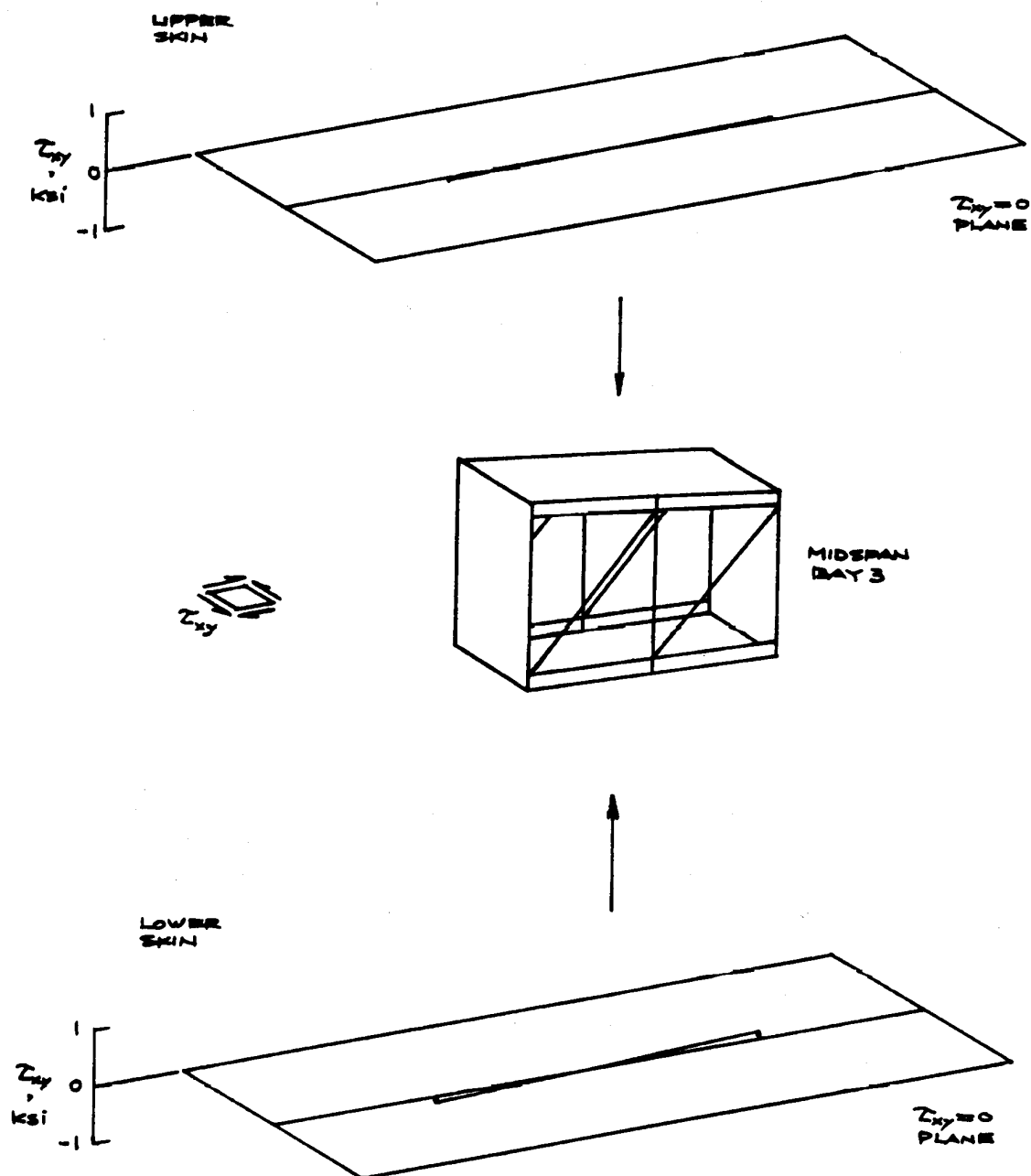*(c) NASTRAN structural model C.*

Figure 13. Continued.
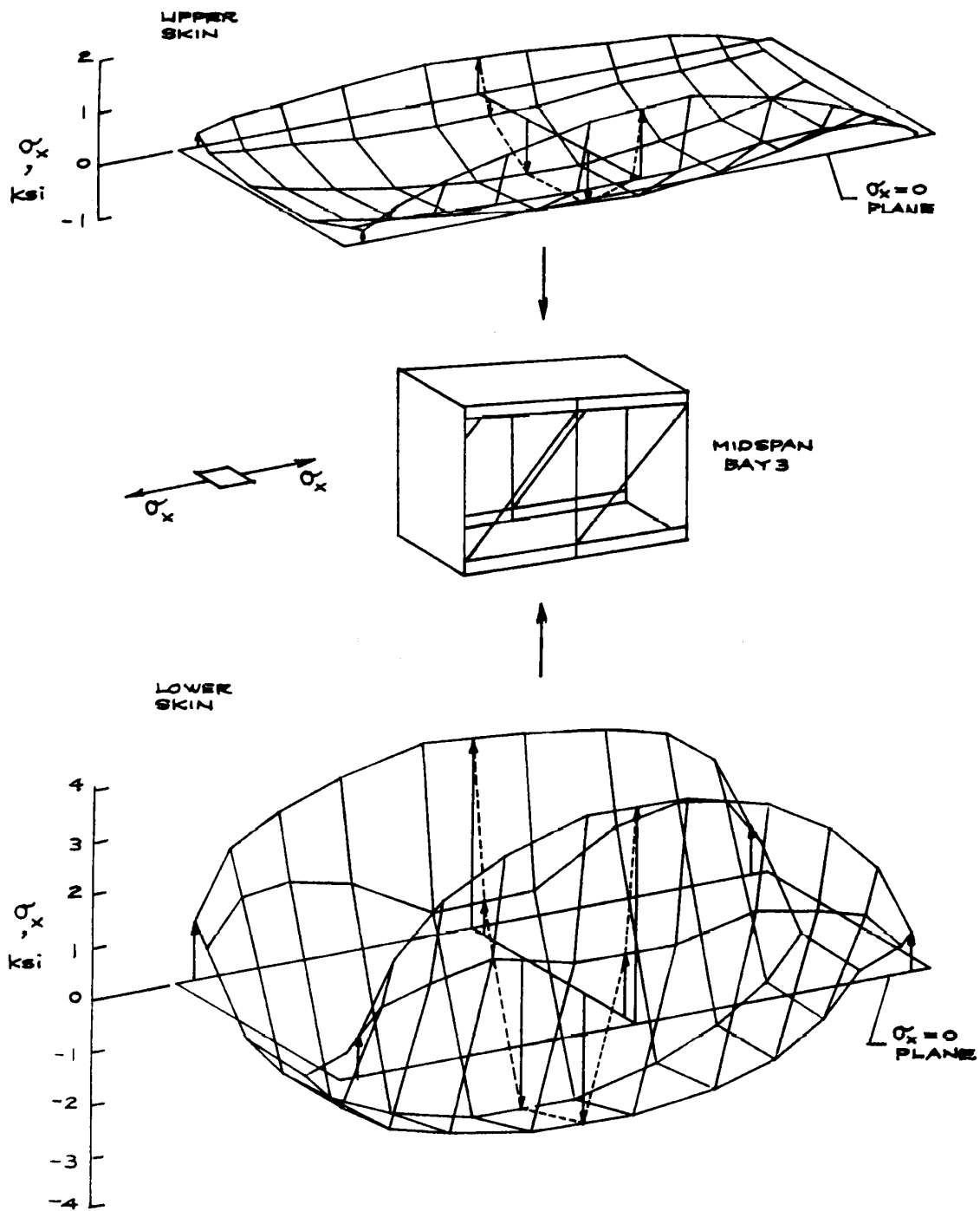
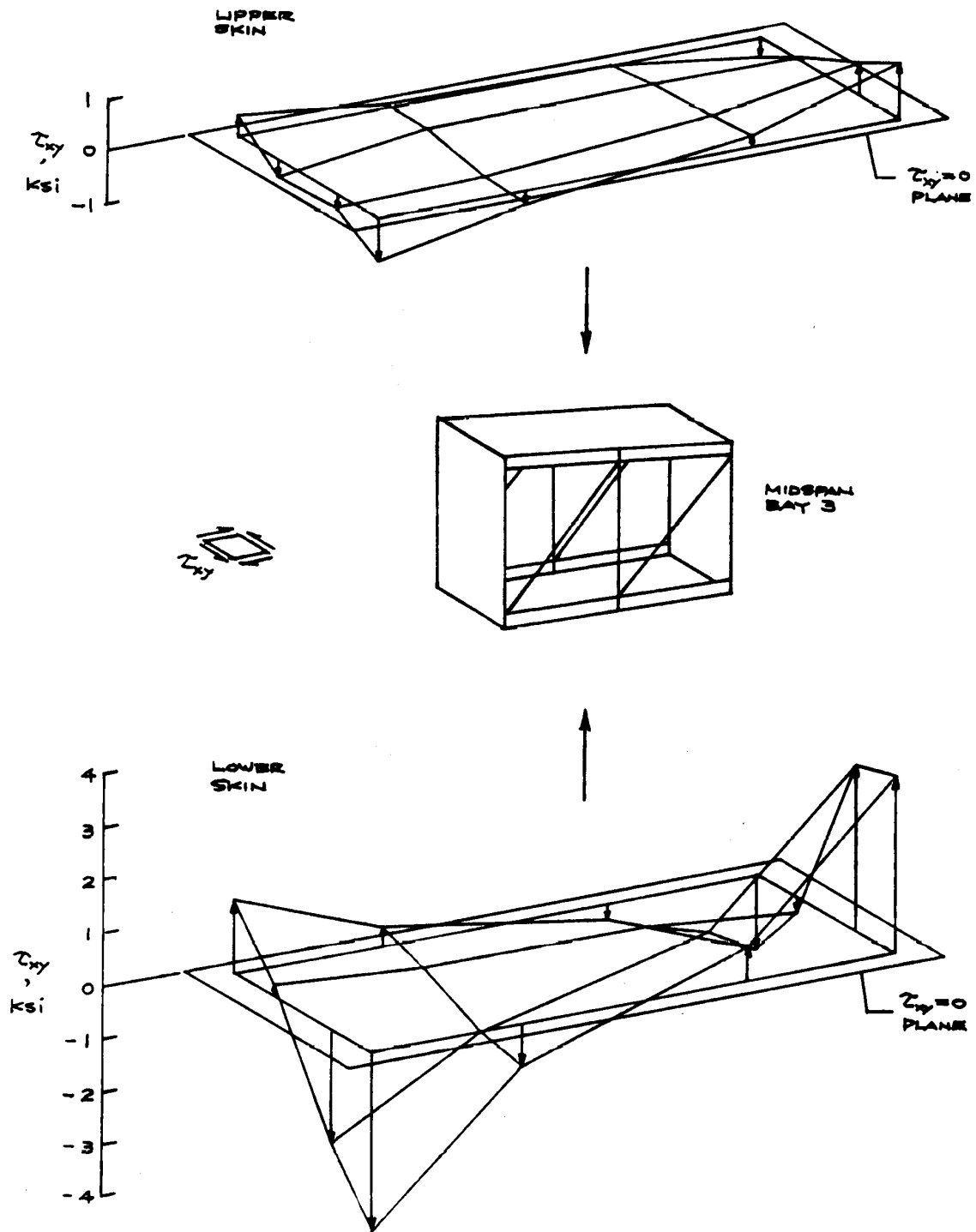(d) NASTRAN structural model D.

Figure 13. Continued.
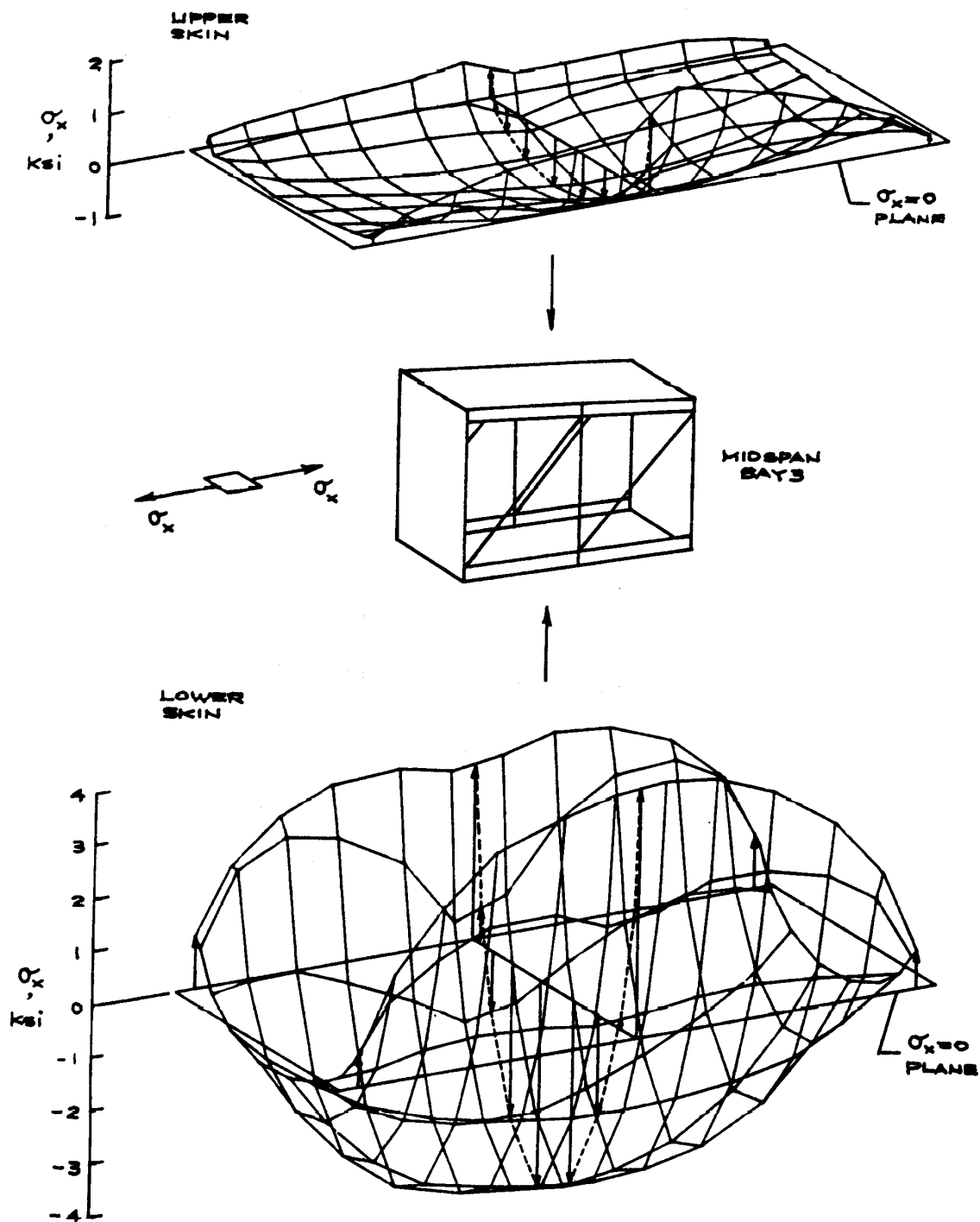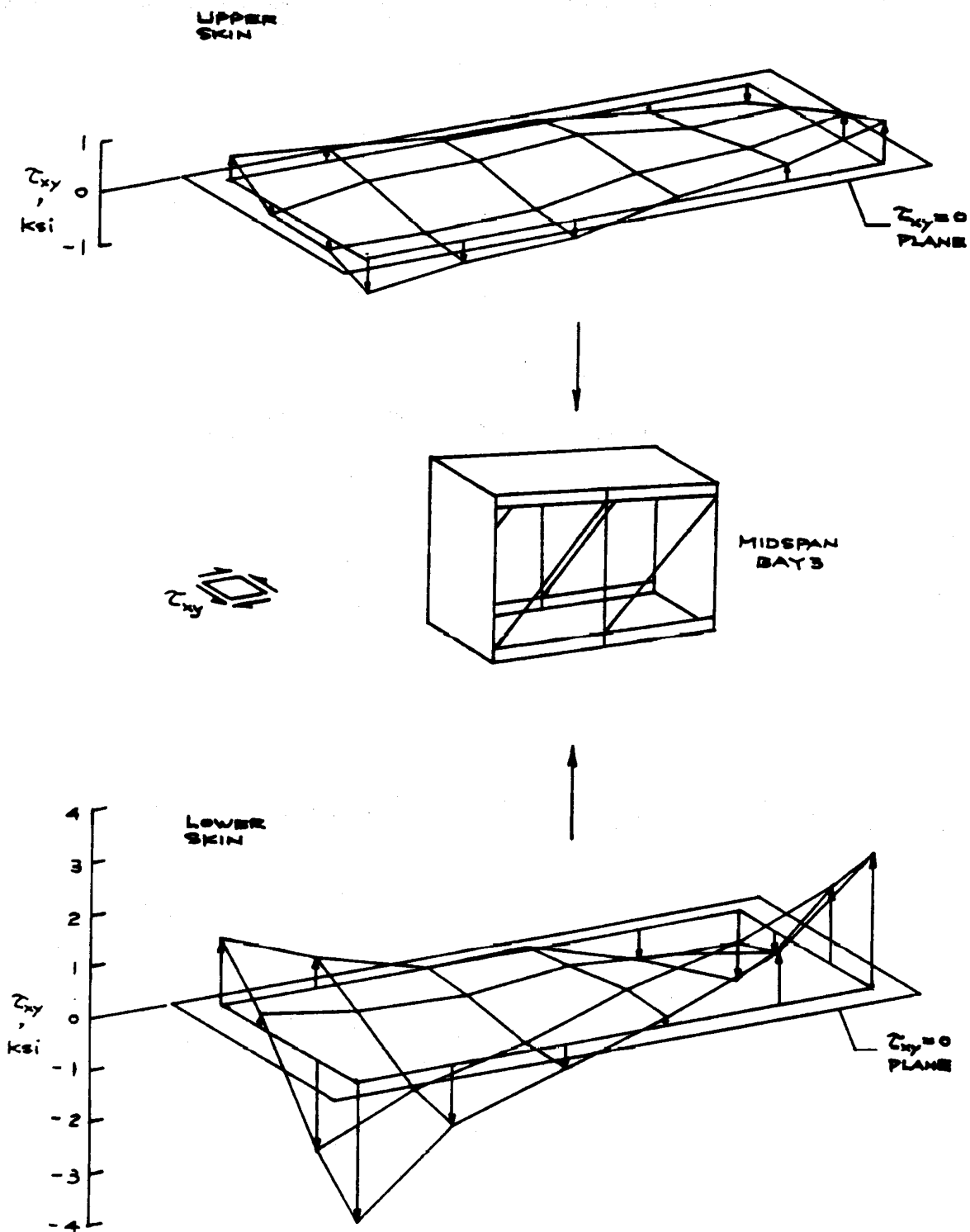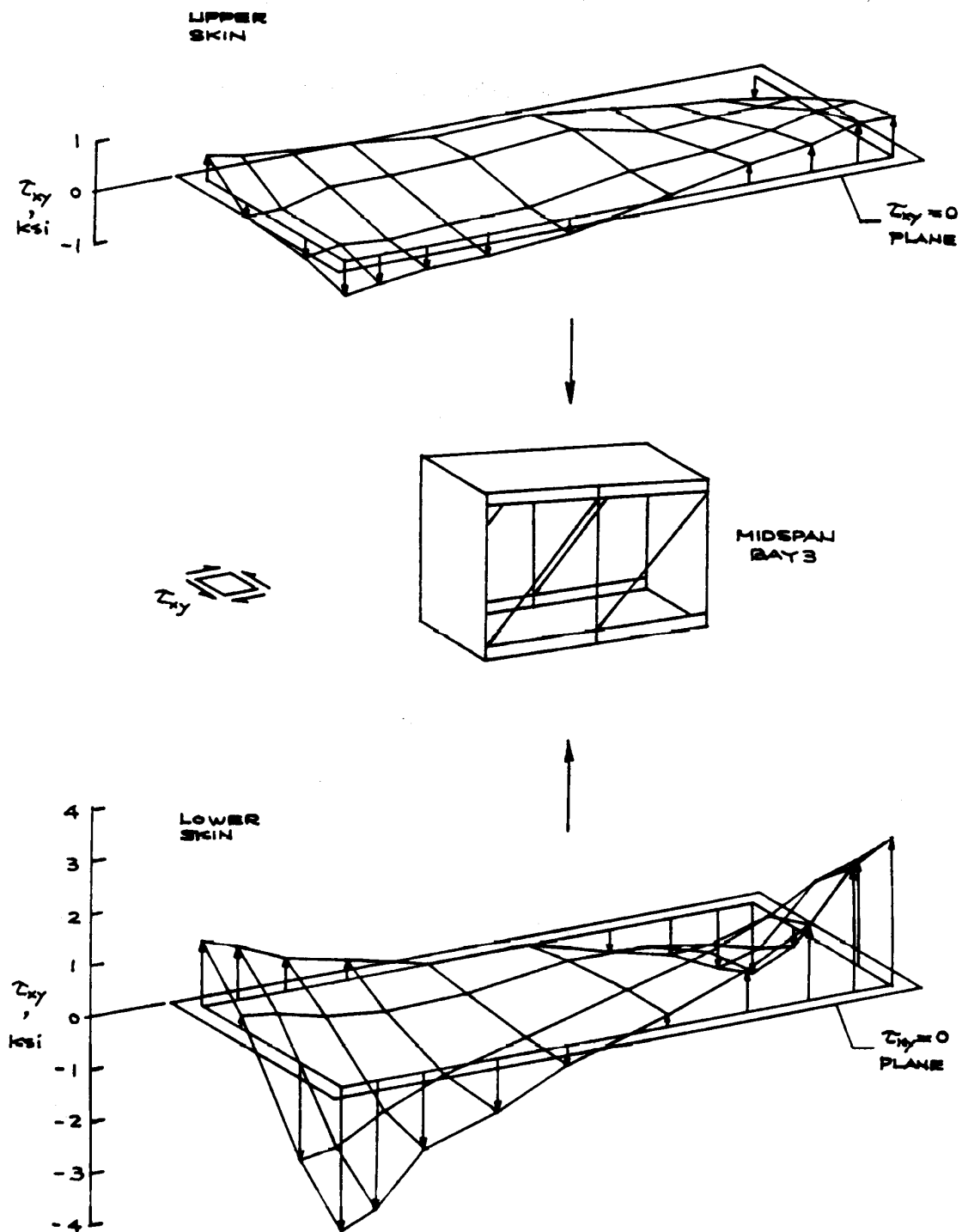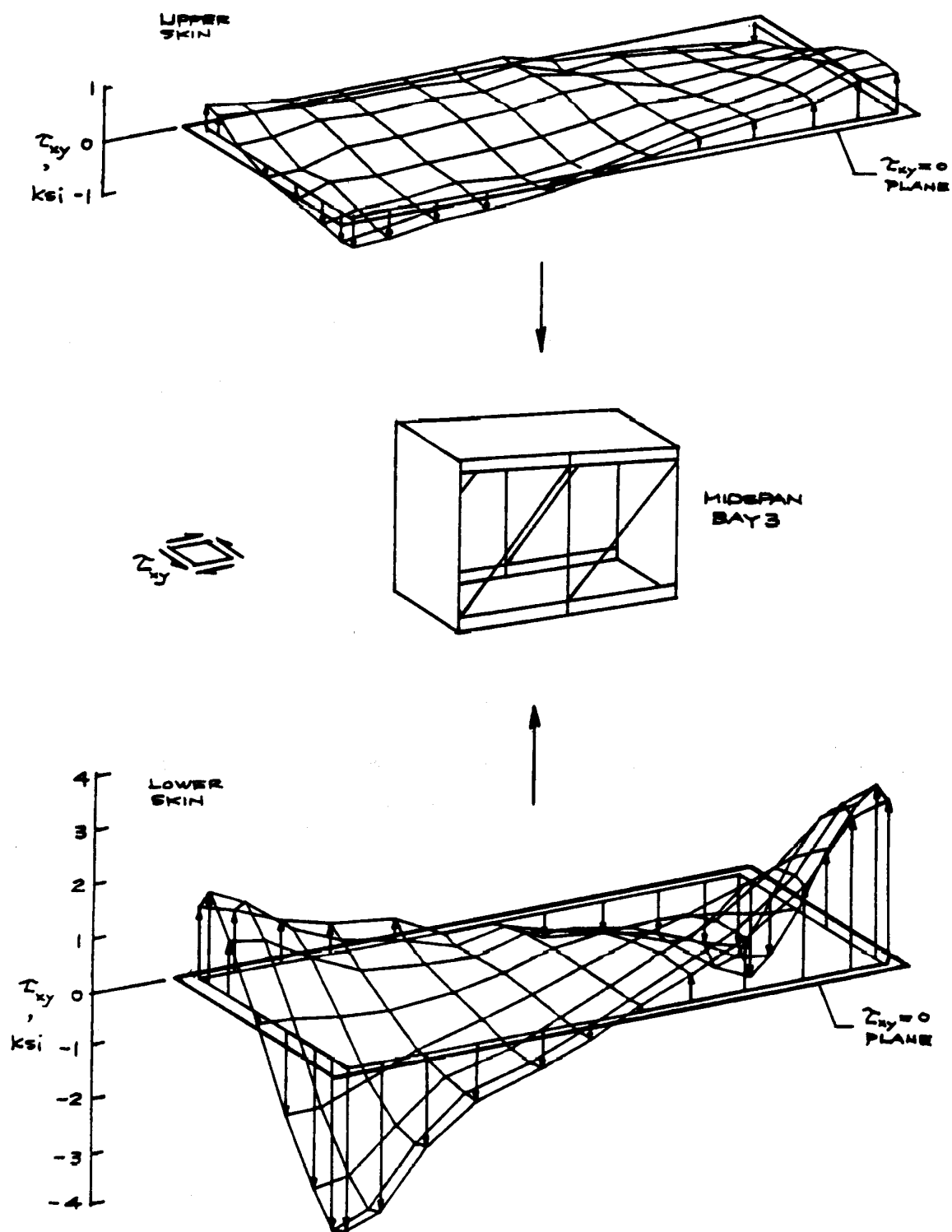
(e) NASTRAN structural model E.

Figure 13. Concluded.
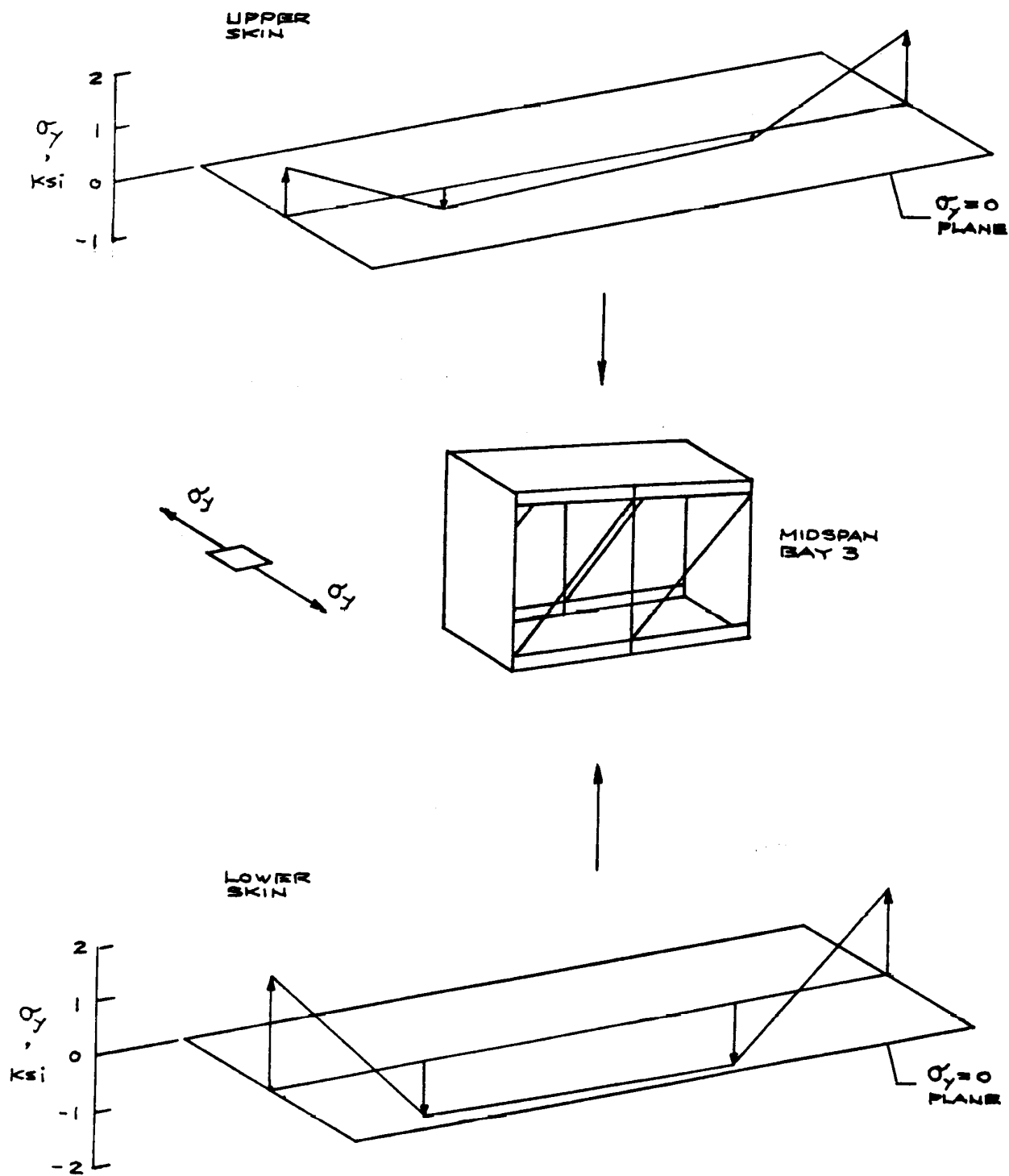
(a) NASTRAN structural model A.

Figure 14. Distributions of spanwise stress σ_y in orbiter wing skins at midspan bay 3; time = 1700 sec, STS-5 flight.
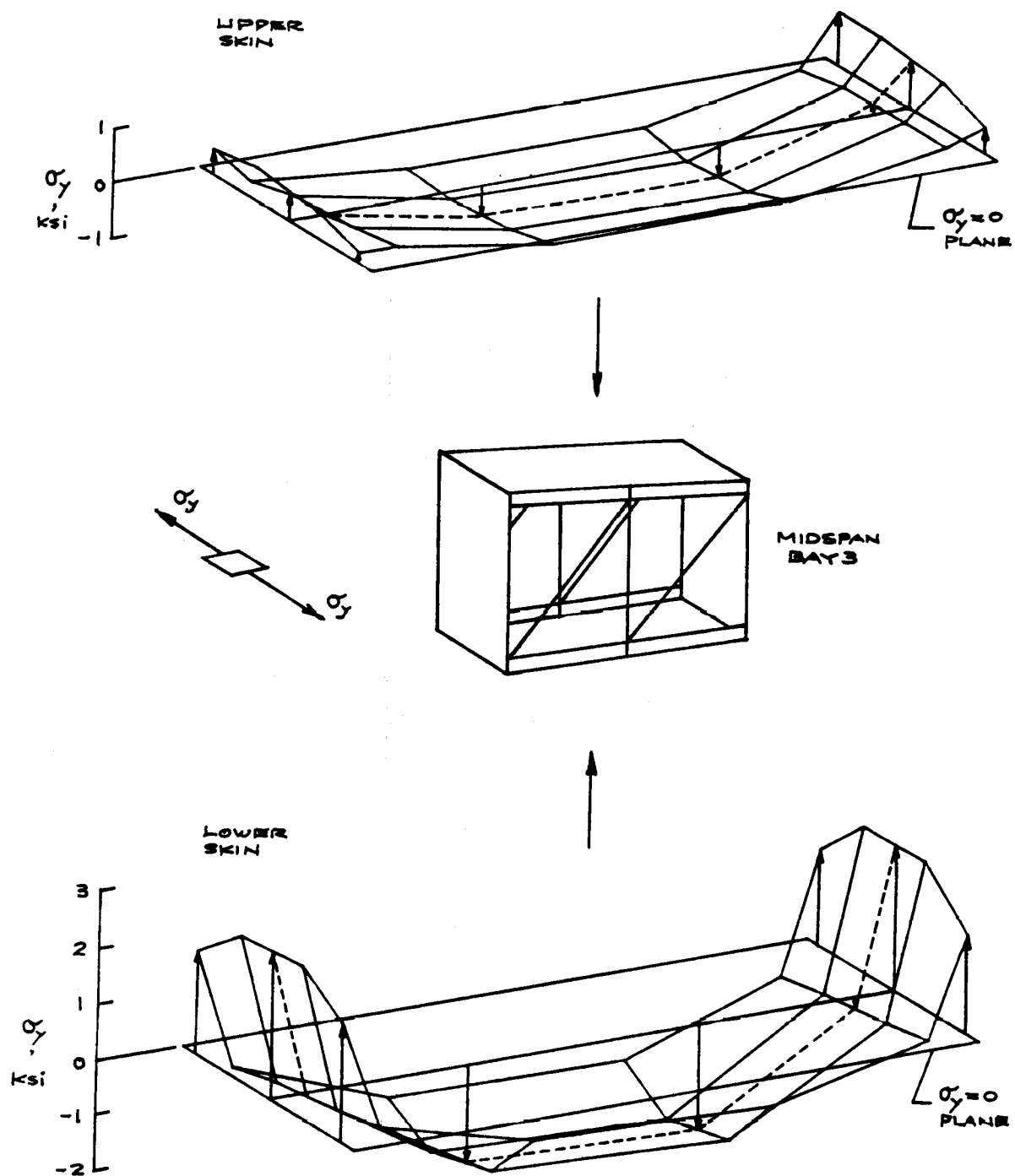
(b) NASTRAN structural model B.

Figure 14. Continued.

UPPER SKIN

σ_y, ksi

$\sigma_y = 0$ PLANE

σ_y

σ_y

MIDSPAN BAY 3

LOWER SKIN

σ_y, ksi
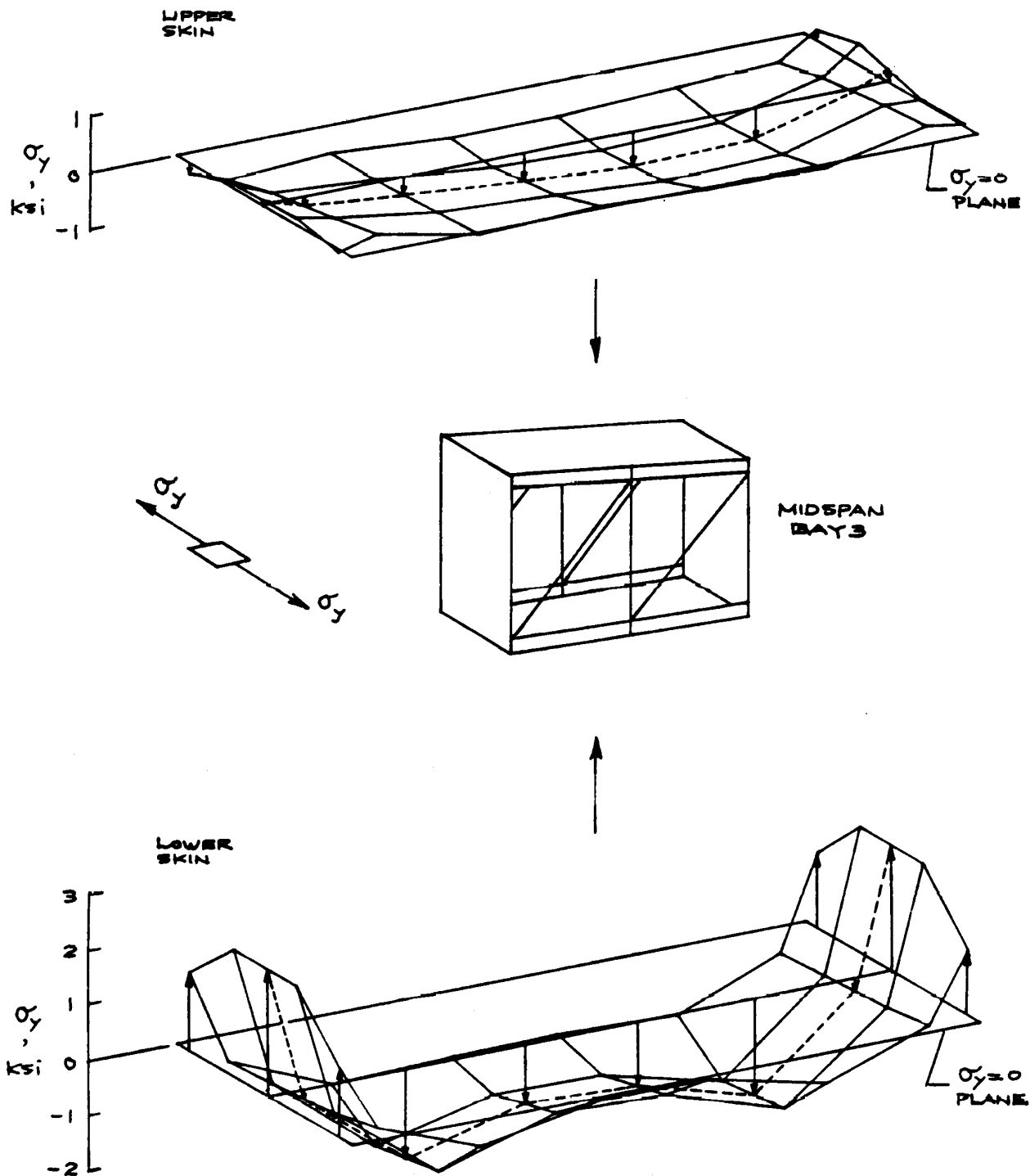
$\sigma_y = 0$ PLANE

(c) NASTRAN structural model C.

Figure 14. Continued.

33

UPPER
SKIN

σ_y, ksi

1
0
-1

$\sigma_y = 0$
PLANE

σ_y

σ_y

MIDSPAN
BAY3

LOWER
SKIN

σ_y, ksi

3
2
1
0
-1
-2

$\sigma_y = 0$
PLANE

(d) NASTRAN structural model D.

Figure 14. Continued.

UPPER
SKIN

σ_y, ksi

1

0

-1

$\sigma_{y=0}$ PLANE

σ_y

σ_y

MIDSPAN
BAY 3

LOWER
SKIN

σ_y, ksi

3

2

1

0

-1

-2

STRESS
INCREASE
ZONE

STRESS
RELEASE
ZONE

$\sigma_{y=0}$ PLANE

(e) NASTRAN structural model E.

Figure 14. Concluded.

35

(a) NASTRAN structural model A.

Figure 15. Distributions in the Y_0-240 plane of shear stress τ_{xy} in orbiter wing skins at midspan bay 3; time = 1700 sec, STS-5 flight.

(b) NASTRAN structural model B.

Figure 15. Continued.

(c) NASTRAN structural model C.

Figure 15. Continued.

(d) NASTRAN structural model D.

Figure 15. Continued.

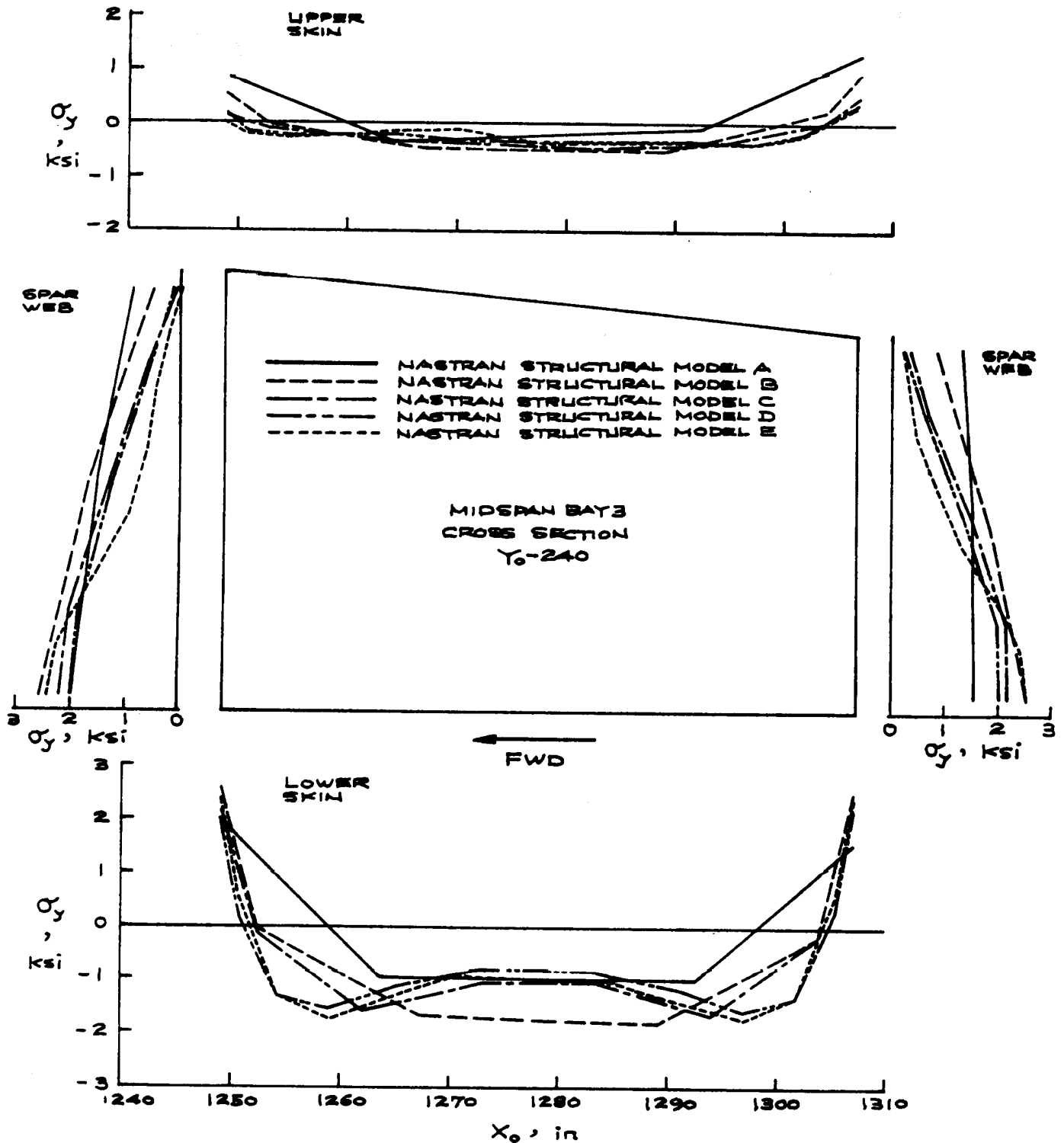(e) NASTRAN structural model E.

Figure 15. Concluded.

Figure 16. Distributions of spanwise stress σ_y in orbiter wing midspan bay 3 calculated using different NASTRAN structural models; time = 1700 sec, STS-5 flight.
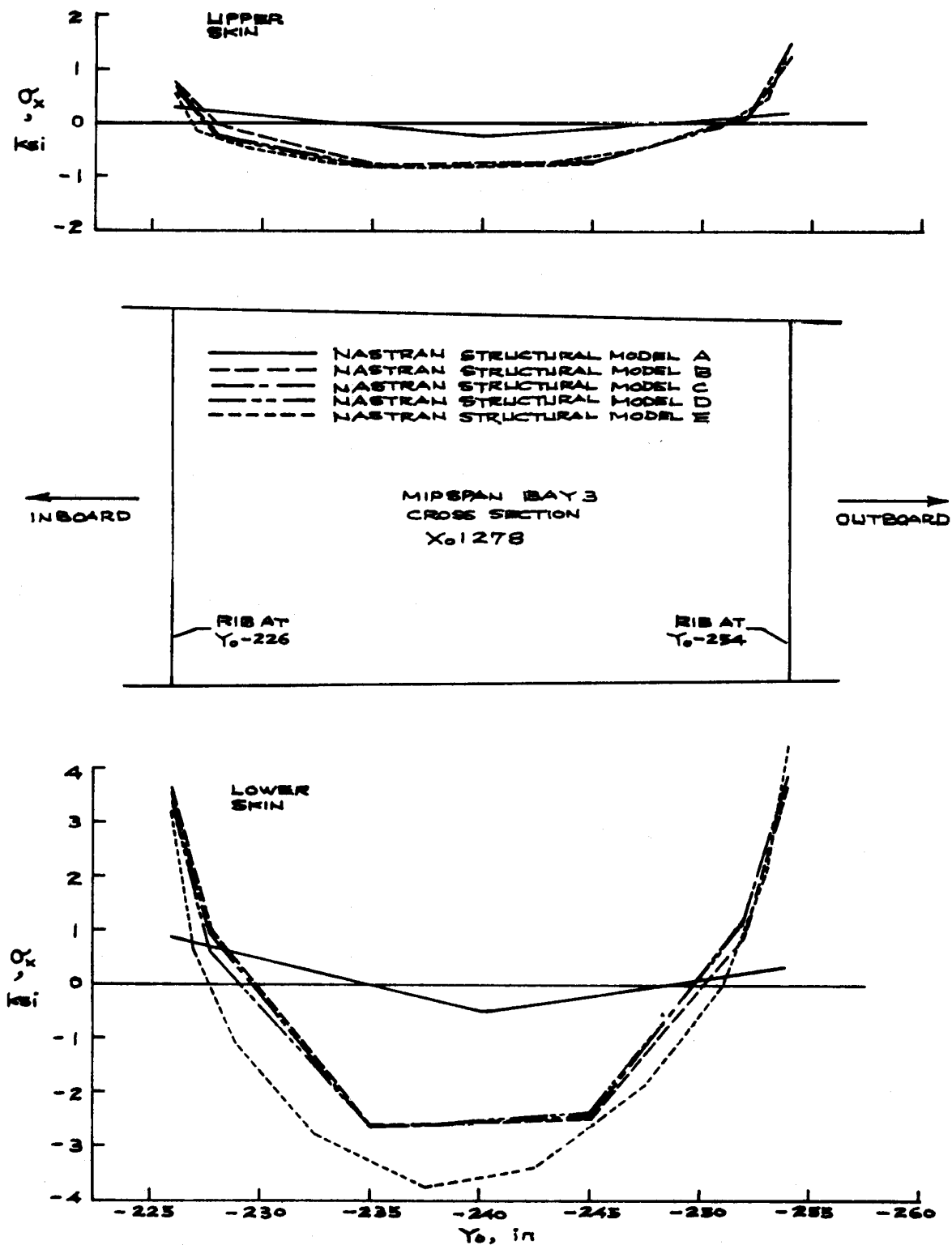
Figure 17. Distributions in the $X_0 1278$ plane of chordwise stress σ_x in orbiter wing midspan bay 3 calculated using different NASTRAN structural models; time $= 1700$ sec, STS-5 flight.
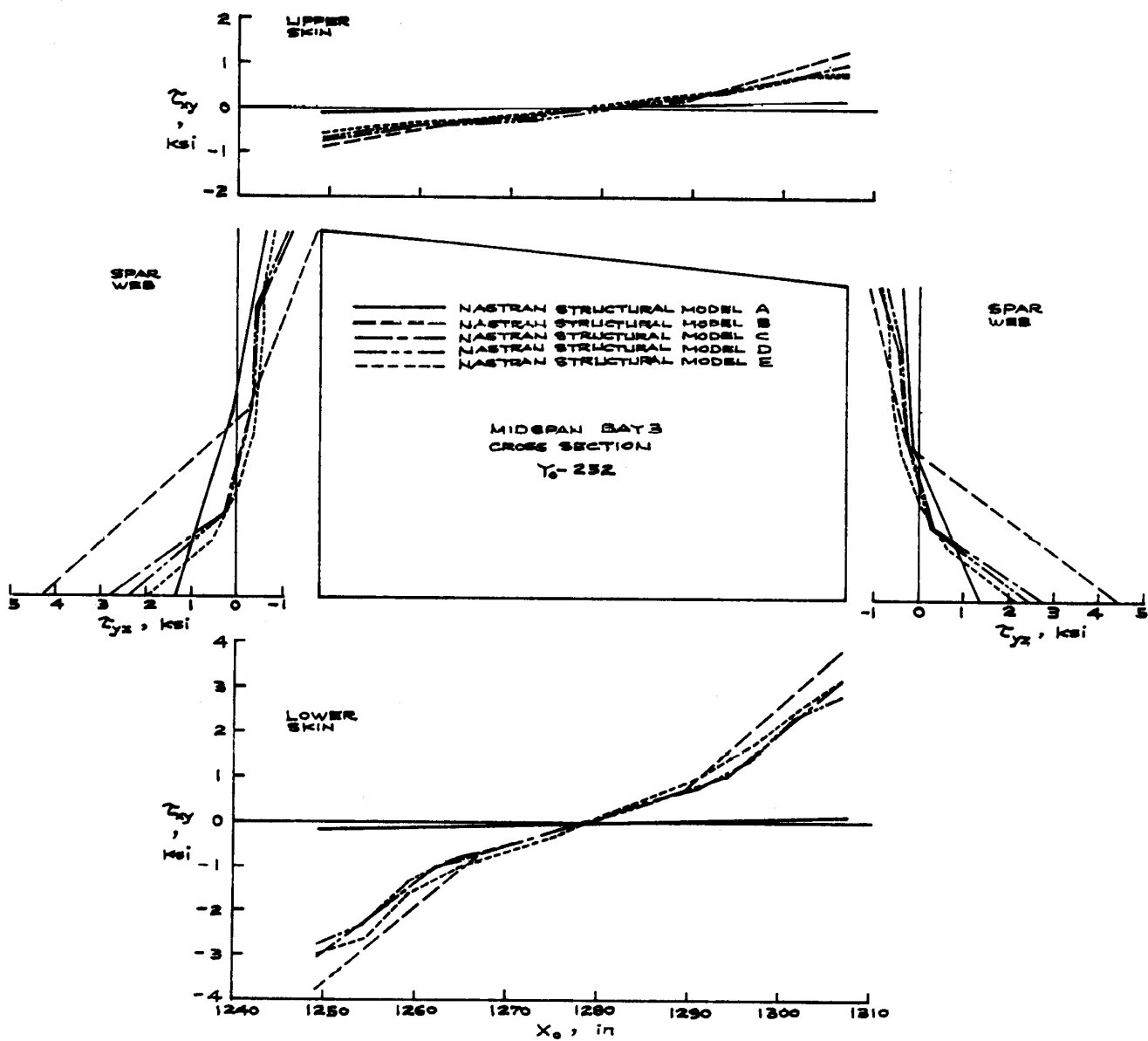
Figure 18. Distributions in the Y_0-252 plane of shear stresses τ_{xy} and τ_{yz} in orbiter wing midspan bay 3 calculated using different NASTRAN structural models; time = 1700 sec, STS-5 flight.
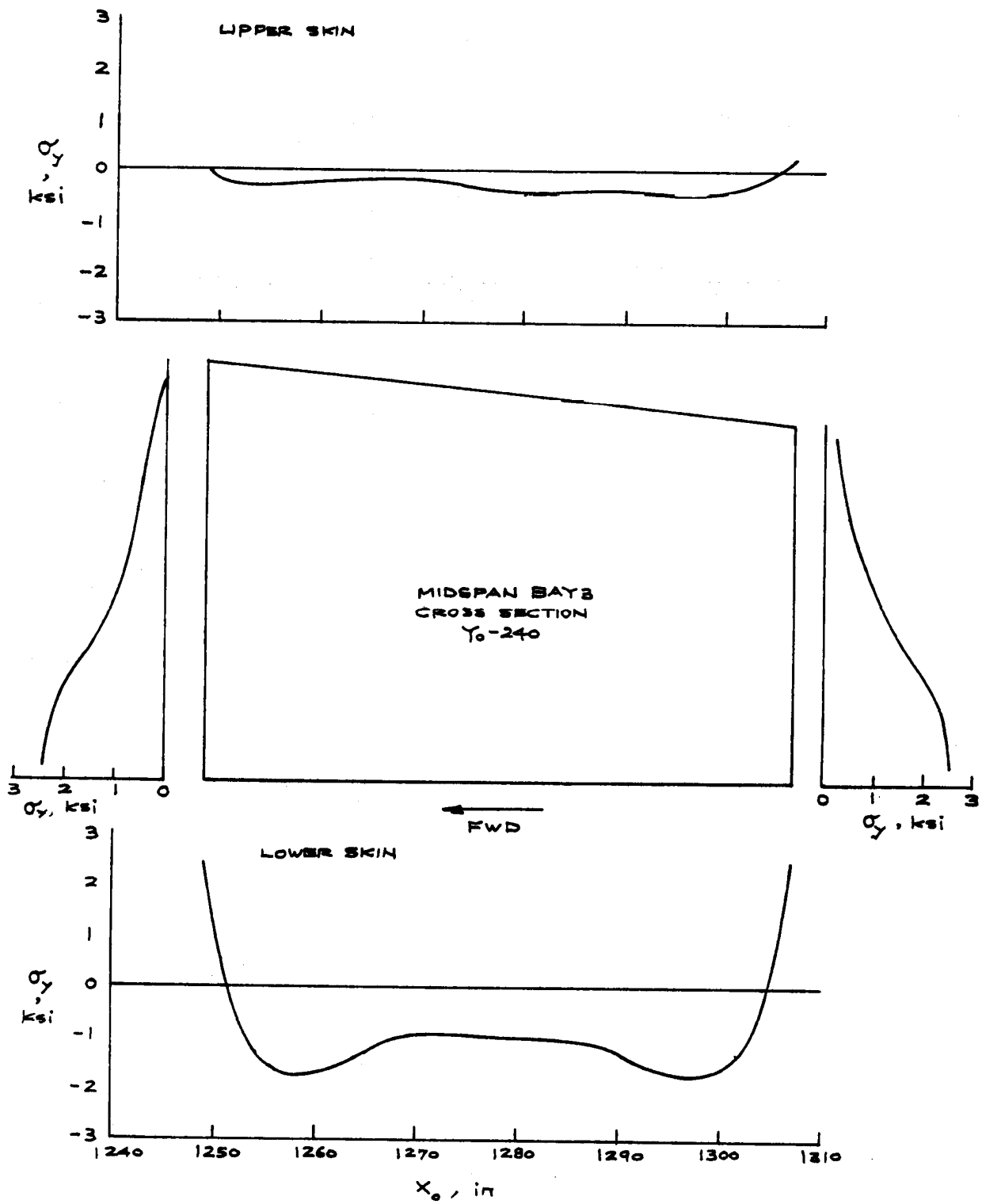
Figure 19. Continuous distributions in the Y_0-240 plane of spanwise stress σ_y based on NASTRAN structural model E: time = 1700 sec, STS-5 thermal loading.
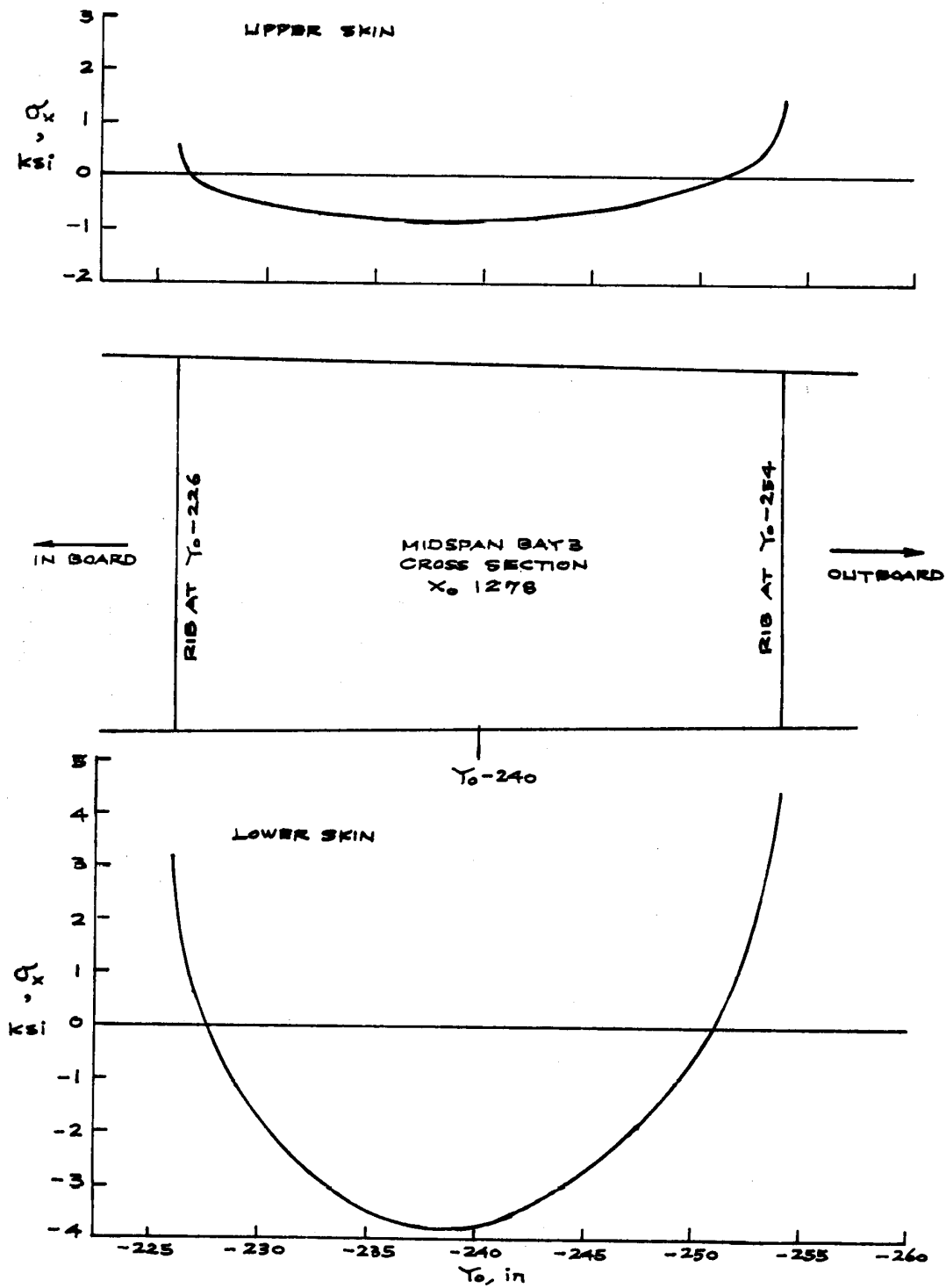
44

Figure 20. Continuous distributions in the X_01278 plane of chordwise stress σ_x based on NASTRAN structural model E; time = 1700 sec, STS-5 thermal loading.
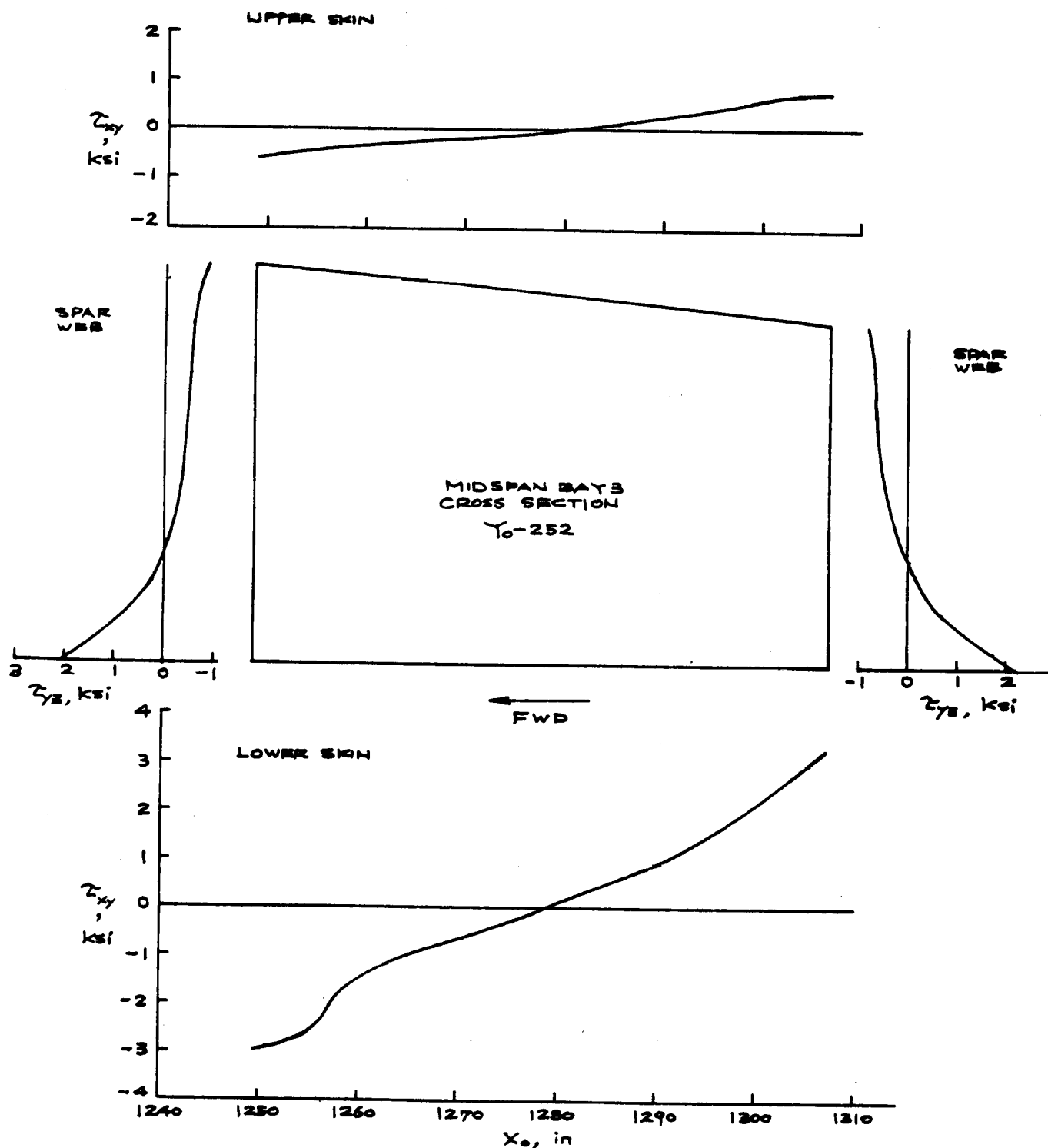
Figure 21. Continuous distributions in the Y_0-252 plane of shear stresses τ_{xy} and τ_{yz} based on NASTRAN structural model E; time = 1700 sec, STS-5 thermal loading.
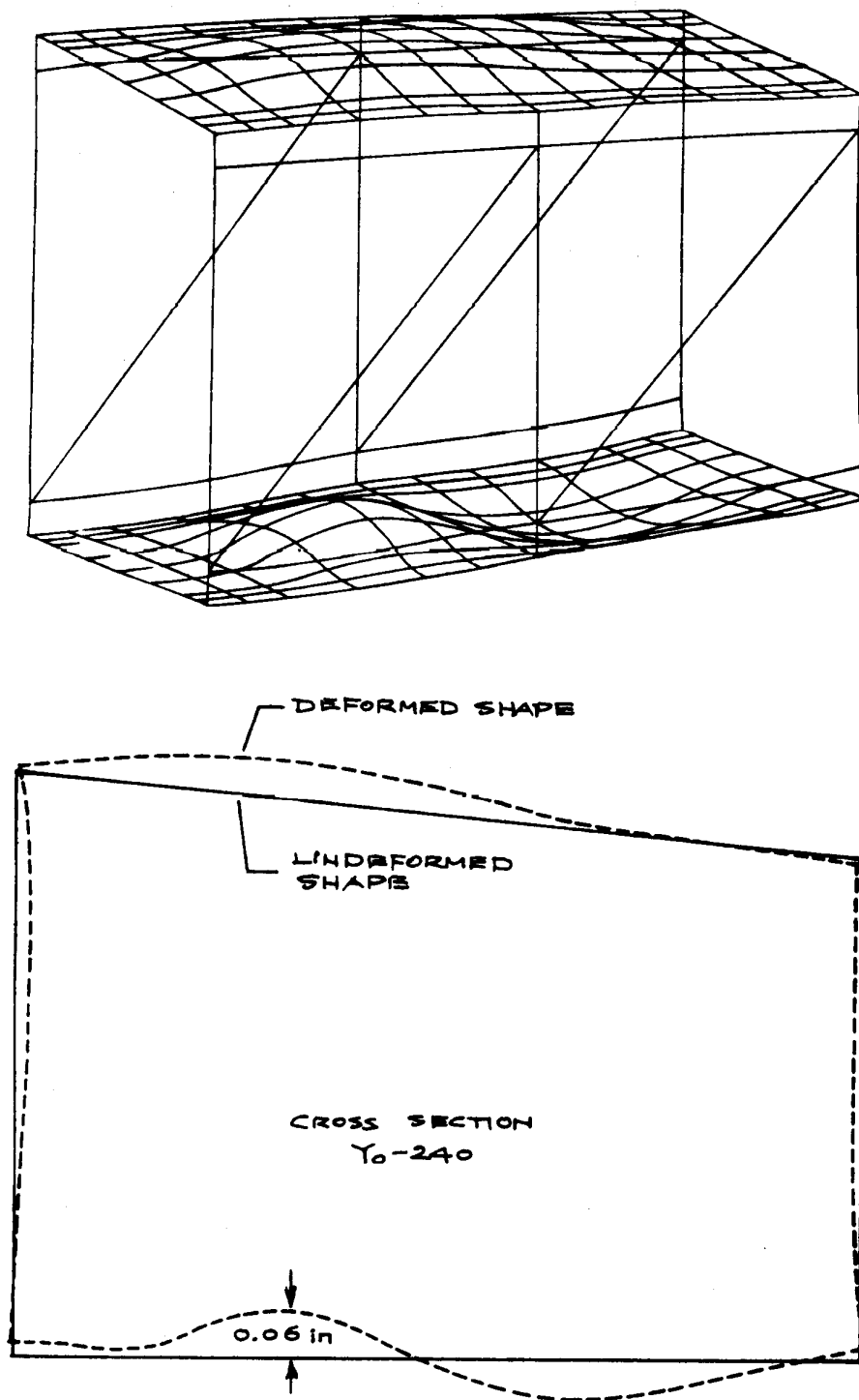
Figure 22. Deformed shape of orbiter wing midspan bay 3 due to STS-5 thermal loading (dimension in inches); time = 1700 sec.
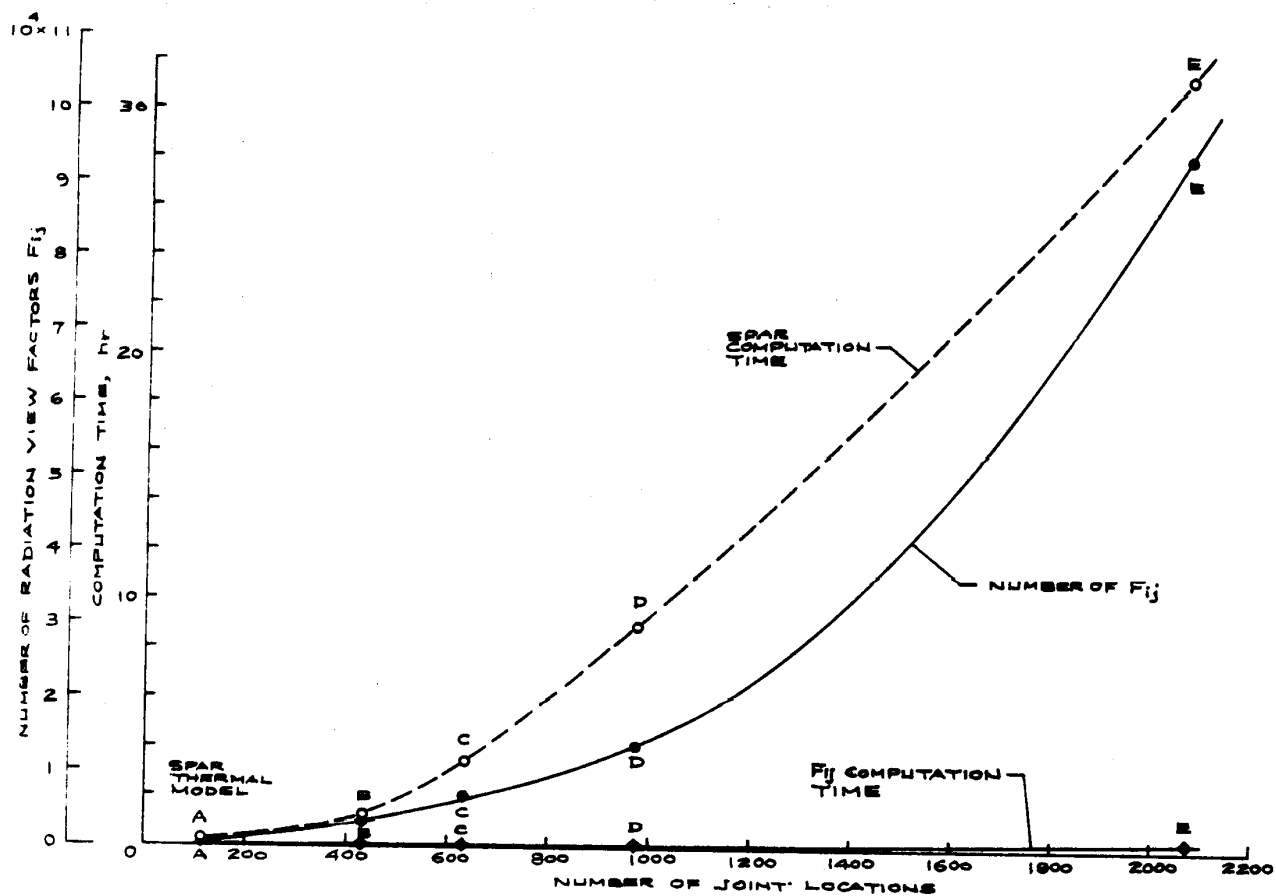
Figure 23. Plots of number of radiation view factors F_{ij} and SPAR computation time as functions of number of joint locations.

1. Report No. NASA TM-88272	2. Government Accession No.	3. Recipient's Catalog No.
4. Title and Subtitle Effect of Element Size on the Solution Accuracies of Finite-Element Heat Transfer and Thermal Stress Analyses of Space Shuttle Orbiter		5. Report Date August 1987
		6. Performing Organization Code
7. Author(s) William L. Ko and Timothy Olona		8. Performing Organization Report No. H-1409
		10. Work Unit No. RTOP 505-53-51
9. Performing Organization Name and Address NASA Ames Research Center Dryden Flight Research Facility P.O. Box 273, Edwards, CA 93523-5000		11. Contract or Grant No.
		13. Type of Report and Period Covered Technical Memorandum
12. Sponsoring Agency Name and Address National Aeronautics and Space Administration Washington, DC 20546		14. Sponsoring Agency Code

15. Supplementary Notes

This report is a revised version of a paper prepared for presentation at the Fifth International Conference on Numerical Methods in Thermal Problems, Montreal, Canada, June 24–July 3, 1987.

16. Abstract

The effect of element size on the solution accuracies of finite-element heat transfer and thermal stress analyses of space shuttle orbiter was investigated. Several structural performance and resizing (SPAR) thermal models and NASA structural analysis (NASTRAN) structural models were set up for the orbiter wing midspan bay 3. The thermal model was found to be the one that determines the limit of finite-element fineness because of the limitation of computational core space required for the radiation view factor calculations. The thermal stresses were found to be extremely sensitive to a slight variation of structural temperature distributions. The minimum degree of element fineness required for the thermal model to yield reasonably accurate solutions was established. The radiation view factor computation time was found to be insignificant compared with the total computer time required for the SPAR transient heat transfer analysis.

17. Key Words (Suggested by Author(s)) Finite elements; Heat transfer; Reentry heating; Solution accuracies; Space shuttle orbiter; Structural modeling; STS-5 flight data; Thermal stresses	18. Distribution Statement Unclassified — Unlimited Subject category 39		
19. Security Classif. (of this report) Unclassified	20. Security Classif. (of this page) Unclassified	21. No. of Pages 49	22. Price* A03

*For sale by the National Technical Information Service, Springfield, Virginia 22161.